JOURNAL OF AIRCRAFT
Vol. 45, No. 3, May–June 2008

Abridged Summary of the Third AIAA Computational Fluid Dynamics Drag Prediction Workshop

John C. Vassberg,* Edward N. Tinoco,* and Mori Mani*
The Boeing Company, Chicago, Illinois 60606-1596
Olaf P. Brodersen† and Bernhard Eisfeld†
DLR Institute of Aerodynamics and Flow Technology, 38108 Braunschweig, Germany
Richard A. Wahls‡ and Joseph H. Morrison§
NASA Langley Research Center, Hampton, Virginia 23681
Tom Zickuhr¶ and Kelly R. Laflin¶
Cessna Aircraft Company, Wichita, Kansas 67218
and
Dimitri J. Mavriplis**
University of Wyoming, Laramie, Wyoming 82071

DOI: 10.2514/1.30572

Results from the Third AIAA Drag Prediction Workshop (DPW-III) are summarized. The workshop focused on the prediction of both absolute and differential drag levels for wing-body and wing-alone configurations that are representative of transonic transport aircraft. The baseline DLR-F6 wing-body geometry, previously used in DPW-II, is also augmented with a side-of-body fairing to help reduce the complexity of the flow physics in the wing-body juncture region. In addition, two new wing-alone geometries have been developed for DPW-III. Numerical calculations are performed using industry-relevant test cases that include lift-specific and fixed-alpha flight conditions, as well as full drag polars. Drag, lift, and pitching-moment predictions from numerous Reynolds-averaged Navier–Stokes computational fluid dynamics methods are presented, focused on fully turbulent flows. Solutions are performed on structured, unstructured, and hybrid grid systems. The structured grid sets include point-matched multiblock meshes and overset grid systems. The unstructured and hybrid grid sets are composed of tetrahedral, pyramid, and prismatic elements. Effort was made to provide a high-quality and parametrically consistent family of grids for each grid type about each configuration under study. The wing-body families are composed of a coarse, medium, and fine grid, whereas the wing-alone families also include an extra-fine mesh. These mesh sequences are used to help determine how the provided flow solutions fare with respect to asymptotic grid convergence, and are used to estimate an absolute drag for each configuration.

Nomenclature

AR	=	wing aspect ratio $=b^2/S_{\text{ref}}$
a	=	acoustic speed
b	=	wing span
C_D	=	3-D drag coefficient $=\text{drag}/q_\infty S_{\text{ref}}$
C_{DP}	=	idealized profile drag $=C_D-(C_L^2/\pi\text{AR})$
$C_{D\text{pr}}$	=	pressure drag coefficient
$C_{D\text{sf}}$	=	skin-friction drag coefficient
C_L	=	lift coefficient $=\text{lift}/q_\infty S_{\text{ref}}$
$C_{L\alpha}$	=	lift curve slope
C_M	=	pitching-moment coefficient
C_P	=	pressure coefficient $=(P-P_\infty)/q_\infty$
C_{ref}	=	wing reference chord $\simeq$ MAC
c_f	=	local coefficient of skin friction
count	=	drag coefficient unit $=0.0001$
N	=	total number of grid points
P	=	static pressure
q	=	dynamic pressure $=\frac{1}{2}\rho V^2$
Re	=	Reynolds number $=\rho_\infty V_\infty C_{\text{ref}}/\mu_\infty$
S_{ref}	=	reference area
T	=	temperature
V	=	velocity
Y^+	=	wall distance $=Re\sqrt{(c_f/2)}y$
α	=	angle of attack
Δ	=	difference in quantity
η	=	fraction of wing semispan
μ	=	fluid viscosity
ρ	=	fluid density
∞	=	signifies freestream conditions

Presented as Paper 0260 at the 45th AIAA Aerospace Sciences Meeting and Exhibit, Reno, NV, 8–11 January 2007; received 20 February 2007; accepted for publication 16 September 2007.

*Boeing Technical Fellow. Associate Fellow AIAA.
†Research Engineer.
‡Assistant Head, Configuration Aerodynamics Branch. Associate Fellow AIAA.
§Research Scientist. Senior Member AIAA.
¶Senior Specialist Engineer. Senior Member AIAA.
**Professor Mechanical Engineering. Associate Fellow AIAA.

I. Introduction

THE AIAA CFD Drag Prediction Workshop (DPW) Series was initiated by a working group of members from the AIAA Applied Aerodynamics Technical Committee. From the onset, the DPW organizing committee defined and has adhered to a set of primary objectives for the DPW series. These include the following:

1) Assess state-of-the-art computational fluid dynamics (CFD) methods as practical aerodynamic tools for the prediction of forces and moments on industry-relevant geometries, with a focus on absolute drag.

2) Provide an impartial international forum for evaluating the effectiveness of CFD Navier–Stokes solvers.

3) Promote balanced participation across academia, government labs, and industry.

4) Use common public-domain subject geometries, simple enough to permit high-fidelity computations.

5) Provide baseline grids to encourage participation and help reduce variability of CFD results.

6) Openly discuss and identify areas needing additional research and development.

7) Conduct rigorous statistical analyses of CFD results to establish confidence levels in predictions.

8) Schedule open-forum sessions to further engage interaction among all interested parties.

9) Maintain a public-domain accessible database of geometries, grids, and results.

10) Document workshop findings and disseminate this information through publications and presentations.

The first workshop [1] in this series, DPW-I , was held in Anaheim, California, in conjunction with the 19th Applied Aerodynamics Conference of June 2001. The premise of DPW-I was to solicit CFD predictions of a common, industry-relevant geometry and assess the results using statistical analysis techniques. Although the focus of the workshop was on drag prediction, lift and pitching-moment predictions were also evaluated. The DLR-F4 wing-body configuration was chosen as the subject of DPW-I both because of its simplicity and the availability of publicly released experimental test data [2]. The workshop committee provided a standard set of multiblock structured, overset, and unstructured grids for the DLR-F4 geometry to encourage participation in the workshop and reduce variability in the CFD results. However, participants were also encouraged to construct their own grids using their *best practices* so that learned knowledge concerning grid generation and drag prediction might be shared [3] among workshop attendees. The test cases were chosen to reflect the interests of industry and included a fixed-C_L single-point solution, drag polar, and constant-C_L drag rise data sets. Eighteen participants submitted results, using 14 different CFD codes; many submitted multiple sets of data exercising different options in their codes, for example, turbulence models and/or different grids. A summary of these results was documented by the DPW-I organizing committee [4,5]. Because of strong participation, DPW-I successfully amassed a CFD data set suitable for statistical analysis [6,7]. However, the results of that analysis were rather disappointing, showing a 270-drag-count spread in the fixed-C_L data, with a 100:1 confidence interval of more than ± 50 drag counts.

Nonetheless, DPW-I was a definitive success. It brought together CFD developers and practitioners and focused their efforts on a common problem. It facilitated an exchange of learned best practices and promoted open discussions, identifying areas requiring further research or additional scrutiny. Possibly most significant, it employed statistical methods to objectively assess CFD results. Finally, it reminded the CFD and applied aerodynamics communities that CFD is not yet a fully matured discipline.

In addition to the accomplishments listed above, DPW-I initiated interest in industry-relevant drag predictions that has been sustained through two more workshops and looks to continue beyond. Several of the participants presented their DPW-I results [8–12] at a well-attended special session of the 2002 AIAA Aerospace Sciences Meeting and Exhibit in Reno, Nevada. The interest generated by DPW-I naturally led to the planning and organization of the 2nd AIAA Drag Prediction Workshop, DPW-II. The DPW-II organizing committee, recognizing the success of DPW-I, maintained its objectives for DPW-II.

The second workshop [13] was held in Orlando, Florida, in conjunction with the 21st Applied Aerodynamics Conference of June 2003. For this workshop, the DLR-F6 was chosen as the subject geometry, in both wing-body (WB) and wing-body-nacelle-pylon (WBNP) form. The DPW-II organizing committee worked with DLR and ONERA to make pertinent experimental data available to the public domain. One specific objective of DPW-II was the prediction of the incremental drag associated with nacelle/pylon installation. Although the F6 geometry is similar to that of the F4, its pockets of flow separation at the design condition are more severe; these occur predominantly at the wing/body and wing/pylon juncture regions. Again, this workshop was documented with a summary paper [14,15], a statistical analysis [16], an invited reflections paper [17] on the workshop series, and numerous participant papers [18–30] in two special sessions of the 2004 AIAA Aerospace Sciences Meeting in Reno, Nevada. A conclusion of DPW-II was that the separated flow regions made it difficult to draw meaningful conclusions with respect to grid convergence and drag prediction. During the follow-up open-forum discussions, the CFD community voiced the desire for the organizing committee to include in the third workshop: 1) *blind test cases*, and 2) *simpler geometries*. The request for blind test cases is motivated by an earnest attempt to better establish a measure of the CFD community's capability to predict absolute drag, rather than match it after the fact. The request for simpler geometries allows more extensive research in studies of asymptotic grid convergence.

The third workshop [31] was held in San Francisco, California, in conjunction with the 24th Applied Aerodynamics Conference of June 2006. The DLR-F6 WB from DPW-II was retained as a baseline configuration for the DPW-III to provide a bridge between these two workshops. However, to test the hypothesis that the grid-convergence issues of DPW-II were the direct result of the large pockets of flow separation, a new wing-body fairing was designed to eliminate the side-of-body separation. Details of the FX2B fairing design are documented by Vassberg et al. [32]. In addition, to help reduce the wing upper-surface trailing-edge flow separation, a higher Reynolds number was introduced for the WB test cases. These changes in both geometry and flow condition also provided the DPW-III participants a blind test because no test data would be available before the workshop. Furthermore, two wing-alone geometries were created to provide workshop participants with simpler configurations on which more extensive grid-convergence studies could be conducted; these wings were designed to not exhibit any appreciable separation at their design conditions. An extended summary paper [33] for this workshop is available.

The DPW-III had a total of 15 participants submit multiple data sets for the DLR-F6 WB cases and 10 participants submit data sets for the wing-alone cases. To illustrate the balance of participation achieved in these workshops, the demographics of the DPW-III breakdown is as follows: 1) USA: 66%, Europe: 21%, Asia: 13%; 2) industry: 54%, government labs: 33%, academia: 13%; 3) structured: 42%, hybrid: 46%, tetrahedra: 12%; 4) returning from DPW-II: 54%, new to DPW: 46%.

In addition to the publications spawned directly by the DPW series, the DPW databases have been used elsewhere and continue to be downloaded from the web site. Two notable references are by Baker [34] and Salas [35]; both provide independent, rigorous analyses of the grid-sensitivity data generated by the DPW-II. The conclusions of these studies were leveraged by the organizing committee to better construct the test cases for DPW-III, and although the applications of the test cases still have flaws, the lessons learned from each workshop *have* improved the outcome of subsequent workshops.

When the concept of this workshop series first began to take form in January of 2000, it was impossible then to imagine the magnitude of the cumulative efforts the DPW participants would be willing to invest. Even in retrospect, this is hard to believe. It is a testament that a grass-roots campaign such as this workshop series can accomplish so much. Through the contributions of the DPW participants, the public now has access to a wealth of previously unavailable CFD data.

This paper is organized in the following manner. Section II provides a description of the subject configurations. Section III outlines the test cases of the third workshop. Section IV gives a brief description of the family of baseline grids used in the workshop. Section V summarizes the collective results of the DPW-III. Section VI provides a status of the wind-tunnel test campaign currently under work to collect experimental data on the DLR-F6 and FX2B WB configurations.

II. Geometry Descriptions

A. DLR-F6 Wing/Body and FX2B Fairing

The baseline WB configuration for DPW-III was the DLR-F6 wing/body which was the same geometry used as the test case in DPW-II. The F6 wind-tunnel model represents an aircraft designed to cruise at transonic speeds with a wing leading-edge sweep of 27.1 deg and a quarter-chord sweep of 25 deg. The dihedral of the wing is 4.787 deg. More reference quantities for this model are as follows: $S_{\text{ref}}/2 = 72,700.0$ mm^2; $C_{\text{ref}} =$ 141.2 mm; $b/2 = 585.647$ mm; $X_{\text{ref}} = 157.9$ mm; $Y_{\text{ref}} =$ 0.0 mm; $Z_{\text{ref}} = -33.92$ mm.

Note that an aspect ratio of 9.5 is used herein instead of the computed value of 9.436. The purpose of this is to remain consistent with the literature on this geometry. A planform view of the F6 WB configuration is shown in Fig. 1. For more detailed information on this geometry, see Brodersen [36] and Laflin [14].

The DLR-F6 model has an acute angle, roughly 60 deg, between the fuselage and wing upper surface at the trailing edge which contributes or leads to flow separation at the WB juncture. A new WB fairing was developed by Vassberg et al. [32] with the goal of completely removing the separation bubble present at the design conditions. For consideration of a possible follow-on wind-tunnel test, the only design constraint for this fairing was that it does not cut into the baseline DLR-F6 geometry. Further, no attempt was made to optimize drag reduction. By removing the side-of-body pocket of flow separation, this workshop could test the hypothesis that the complexity associated with flow separations is the root cause of the poor asymptotic grid convergence identified in DPW-II.

B. DPW Wings W1 and W2

Two wing-alone geometries DPW–W1/W2 were developed for DPW-III. Both have a common simple trapezoidal planform shape with no leading-edge or trailing-edge breaks. Their leading-edge sweep is 17.2 deg and they have a quarter-chord sweep of 15.0 deg. Their reference quantities are summarized as follows: $S_{\text{ref}}/2 = 145,161.0$ mm^2; $C_{\text{ref}} = 197.556$ mm; $b/2 = 762.0$ mm; AR $= 8.0$. W1: $X_{\text{ref}} = 6847.145$ mm; $Y_{\text{ref}} = 0.0$ mm; $Z_{\text{ref}} =$ 2226.615 mm. W2: $X_{\text{ref}} = 154.245$ mm; $Y_{\text{ref}} = 0.0$ mm; $Z_{\text{ref}} =$ 0.0 mm.

The airfoil selected for DPW-W1 is representative of a supercritical section found on most modern transport aircraft. At the design condition of Mach 0.76 and $C_L = 0.50$, the upper-surface pressure distribution has a nearly flat, roof-top shape with a shock located at about 57% x/c.

The second wing, DPW-W2, was created by optimizing the first. A Tranair [37] single-point optimization at Mach 0.76 and 5×10^6 Reynolds number was performed on the DPW-W1 wing to create a test for drag increment prediction. Because the goal was to preserve the planform and thickness of the original wing, only camber and twist design variables were used. The variables were laid out at seven spanwise cuts (airfoils), with five camber and one twist variable per airfoil, for a total of 42 geometry degrees of freedom. The twist variable rotates the airfoil about its trailing edge in a plane orthogonal to the y axis. In addition, the angle of attack was allowed to vary to maintain the same lift coefficient at this Mach number as that of the original wing. No attempt was made to tune the locations of the geometry variables. For each airfoil section, camber variables were placed at every 0.2 in x/c, starting at 0.1 and ending at 0.9 x/c. These camber bumps are given by quintic B-splines which interpolate the amplitude of the central knot and vanish at neighboring endpoint knot locations. The defining airfoil sections were placed at 0.0, 0.2, 0.4, 0.6, 0.75, 0.90, and 1.0 in fractions of semispan. This allows the entire wing to change shape, including both the wing root and the wing tip. To prevent a singular problem definition, the twist variable at the wing root was fixed at 0. All variables express a delta change in geometry from the initial wing.

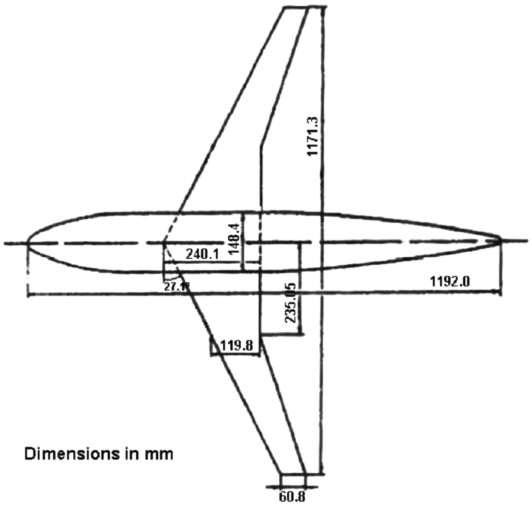

Fig. 1 DLR-F6 wing/body planform.

The optimization used the variables described above to minimize the drag as computed by the farfield formulation of induced, profile, and wave drags. This was subject to the fixed-lift constraint, and a set of transpiration modeling constraints which are necessary to keep the optimization step size within the domain of applicability of the model problem which is constructed on each Tranair grid. The optimizer used was the sequential quadratic programming algorithm, NPSOL [38,39]. The largest camber change was approximately 1.4 mm in full scale units, with the twist change being between ± 0.5 deg.

Additional information regarding the design of these wings is provided by Zickuhr and Tinoco in the workshop presentations [31] on geometry review.

III. Test Cases

The success of the DPW series is due in large part to the significant amount of personal time and computing resources invested by the participants of the workshops. To keep these individual investments from growing out of control, the organizing committee decided to essentially manage DPW-III as two subworkshops within one. Participants were allowed to select one of the following two cases, but were then required to provide all data mandated for that test case. Both cases are blind tests, the first on rather simple wing/body configurations, the second on extremely simple wing-alone shapes. Both cases include a single-point grid-sensitivity study, and an alpha sweep on a medium-size grid. Note that a fixed-lift condition requires convergence on α; this in turn adds additional effort. In addition, the CFD solutions for both test cases were required to represent fully turbulent flow as closely as possible.

To collect a consistent set of data from each participant, the organizing committee supplied template data set files. These templates requested lift, drag (broken down by mechanical component), pitching moment, pressure distributions at specified span stations, trailing-edge separation locations, dimensions of the side-of-body separation bubble, grid family and sizes, turbulence model, computing platform and code performance, number of processors used, number of iterations required, etc. These workshops capture an extensive amount of information that serves as a snapshot of the industry capabilities of the time. For example, in the three workshops held thus far, one obvious trend is that the size of a typical wing/body grid has grown dramatically; the averages of size of the medium WB structured meshes in DPW-I, DPW-II, and DPW-III have been 3.2×10^6, 5.4×10^6, and 7.8×10^6 grid points, respectively. This represents a growth rate of 30% per year between DPW-I and DPW-II, and 13% per year between the last two workshops. Does this indicate that engineering applications are finally approaching the grid resolutions needed for accurate drag predictions on a wing/body configuration? We will at least show that the engineering-class grid resolutions (DPW medium grids) are likely within the asymptotic range of grid convergence for many, yet not all, of the solvers represented herein.

A. Case 1: DLR-F6 WB with and Without FX2B Fairing

The first test case is based on the DLR-F6 wing/body configuration. This case study was constructed to serve two purposes: 1) provide a link to DPW-II, and 2) test a hypothesis that pockets of flow separation can be a root cause for results showing poor grid convergence.

Participants were required to provide data for both the baseline DLR-F6 geometry and one that incorporates the FX2B fairing at the following flow conditions on the specified grids.

Fixed-C_L Single-Point Grid-Sensitivity Study on Three Grids

1) Mach $= 0.75$, $C_L = 0.5$, $Re = 5 \times 10^6$.

Drag Polar on Medium Grid

1) Mach $= 0.75$, $Re = 5 \times 10^6$, $\alpha = [-3.0, -2.0, -1.0, -0.5, 0.0, 0.5, 1.0, 1.5$ deg].

B. Case 2: DPW–W1/W2 Wing Alone

The second test case is based on generic wing-alone geometries designed by members of the organizing committee. Participants were required to provide data for both wings at the following flow conditions on the specified grids.

Fixed-α Single-Point Grid-Sensitivity Study on Four Grids

1) Mach $= 0.76$, $\alpha = 0.5$ deg, $Re = 5 \times 10^6$.

Drag Polar on Medium Grid

1) Mach $= 0.76$, $Re = 5 \times 10^6$, $\alpha = [-1.0, 0.0, 0.5, 1.0, 1.5, 2.0, 2.5, 3.0$ deg].

IV. Baseline Grids

An overview of the baseline grids is provided in this section. However, the details of these grids are not included herein. For more information regarding these grids, please refer to the following companion papers. Tinoco et al. [40] provide descriptions of the Tinoco multiblock structured and advancing-front local-reconnection (AFLR) unstructured grid families. Sclafani et al. [41] provide descriptions of the Sclafani overset structured grid families. Mavriplis [42] provides descriptions of the NASA Langley Research Center (LaRC) unstructured-mesh families. Brodersen et al. [43] provide descriptions of the Deutsche Forschungsanstalt fuer Luft- und Raumfahrt (Institute of Aerodynamics and Flow Technology) (DLR) hybrid mesh families.

Because of the variation of grid types needed, a set of gridding guidelines, listed below, was established to help facilitate the creation of these grids. The gridding guidelines were provided to the persons responsible for generating the baseline grids in an attempt to maintain some level of uniformity across all types of meshes. Note that each grid family is required to include a coarse (C), medium (M), and fine (F) grid; case 2 also required an extra-fine (X) grid. Further, the organizing committee decided that the medium mesh should be representative of current engineering applications of CFD being used to estimate absolute drag levels on similar configurations. For unstructured meshes, the size of the medium mesh is also a function of the intended flow solver. For example, a cell-centered scheme has about 5.5 times the number of unknowns as that of a nodal scheme for a given unstructured tetrahedral mesh, with the ratio being closer to 3.5 for typical hybrid meshes. In the tables that follow, only numbers of grid points are given.

Table 1 provides the number of grid points for each grid family, configuration, and resolution for case 1. The Tinoco through AFLR families were baseline grids provided by the organizing committee and are available to the public domain. (Although not shown in this table, the Tinoco grid family also includes a medium–fine mesh for both wing/body configurations.) The Embraer through the Tohoku University aerodynamic simulation code (TAS) grids were generated by individual participants. The types of meshes used include multiblock (MB), overset (OS), unstructured (UN), and hybrid (HY); the LaRC grid family was used in unstructured and hybrid states (UH). These grids range in size from $2.3–41.1 \times 10^6$ points. Also included in this table is a mapping of the participants who used each grid. The usage key is described in Sec. V.

Table 2 provides the number of grid points for each grid family, configuration, and resolution for case 2. All except the Jameson-FLO code (FLO is the name of the series of CFD methods by Jameson) grid family were provided by the organizing committee and are freely available to the public domain. The Tinoco and JFLO families are multiblock; the Sclafani grid family is overset; the DLR grid family is hybrid; the LaRC and Raytheon grid families are unstructured tetrahedral, although these meshes can be converted to hybrid. Case 2 families include an extra-fine mesh in the sequence. The grids range in size from $0.95–55.0 \times 10^6$ points.

Gridding Guidelines

1) Boundary layer region

$Y^+ \leq (1, \frac{2}{3}, \frac{4}{9}, \frac{8}{27})$ (C, M, F, X)

$\Delta_1 \sim 0.0006$ mm (approximate dimensional spacing for $Y^+ = 1$)

$\Delta_2 = \Delta_1$ (two cell layers of constant spacing at viscous wall)

growth rates ≤ 1.25 (preferably ≤ 1.20)

2) Farfield: $\sim 100\ C_{\text{ref}}$ lengths away from geometry

3) Local spacings on medium grid

chordwise: 0.1% local chord at wing leading edge and trailing edge

spanwise: 0.1% semispan at root and tip

cell size on fuselage nose and tail: 2% C_{ref}

4) Cells across wing trailing-edge base: (8, 12, 16, 24) (C, M, F, X)

5) Grid family

medium mesh representative of current engineering drag predictions

maintain a parametric family of uniformly refined grids in sequence

grid size to grow $\sim$3X for each level refinement (structured: 1.5X in each I, J, K direction

give consideration to multigridable dimensions on structured meshes

sample size for DLR-F6 wing/body: $(2.7M, 8M, 24M)$ (C, M, F)

Table 1 Case 1 DLR-F6/FX2B grids—number of grid points

		DLR-F6			FX2B			
Family	Type	Fine	Medium	Coarse	Fine	Medium	Coarse	Usage
Tinoco	MB	27,185,664	8,080,896	2,298,880	27,185,664	8,080,896	2,298,880	A-C, G-J
SAUNA	MB	9,761,201	4,731,073	2,551,989	9,761,201	4,731,073	2,551,989	D
Extruded	MB	28,367,120	9,343,009	2,996,626	28,367,120	9,329,185	3,028,420	E
Gridgen	MB	27,982,776	8,927,196	2,739,621	27,982,776	9,138,772	2,842,878	F, T
Sclafani	OS	26,892,352	7,985,236	2,387,918	26,969,192	8,020,348	2,395,170	K-M, U
DLR	HY	8,535,263	5,102,446	2,464,385	10,305,876	6,111,664	2,873,102	N
ANSYS	HY	18,120,772	8,038,922	3,059,189	20,472,520	8,272,308	3,163,605	O
LaRC	UH	40,014,934	14,298,135	5,354,214	41,069,036	14,598,610	5,618,073	P, Q
AFLR	UN	11,374,451	3,792,485	1,492,082	11,849,212	3,178,559	1,640,590	R, S, Y
Embraer	UN	24,030,000	8,320,000	3,550,000	24,030,000	8,320,000	3,550,000	V
STAR	UN	——	12,377,058	——	21,509,137	12,469,599	8,421,799	W
USM3D	UN	——	——	——	——	——	——	X
TAS	UN	17,535,215	9,431,154	5,399,929	17,219,535	9,481,477	5,422,128	Z

Table 2 Case 2 DPW–W1/W2 grids—number of grid points

	DPW-W1				DPW-W2			
Family	Extra Fine	Fine	Medium	Coarse	Extra Fine	Fine	Medium	Coarse
Tinoco	14,811,489	8,620,123	4,204,203	1,602,651	14,811,489	8,620,123	4,204,203	1,602,651
Sclafani	55,014,321	16,265,909	4,856,149	1,442,285	55,014,321	16,265,909	4,856,149	1,442,285
DLR	17,053,510	10,150,588	5,288,507	2,174,364	16,631,805	9,910,645	5,030,379	1,928,405
LaRC	36,956,019	11,492,625	4,495,117	1,818,508	38,462,630	11,903,329	4,658,853	1,882,672
Raytheon	12,748,678	6,138,245	2,417,082	983,633	12,419,567	5,963,713	2,325,884	947,409
JFLO	——	——	——	——	——	——	——	——

Table 3 Case 1 submissions

Tag	Code	Grid type	Grid family	Turbulence model	Submitter
A	PAB3D	Multiblock	Tinoco	Girimaji EASM	ASM Elmiligui
B	PAB3D	Multiblock	Tinoco	K-Epsilon	ASM Elmiligui
C	PAB3D	Multiblock	Tinoco	SZL EASM	ASM Elmiligui
D	STAR-CCM+	Multiblock	SAUNA	Wilcox K-Omega	QinetiQ Milne
E	UPACS	Multiblock	Extruded	Modified SA	JAXA Murayama
F	UPACS	Multiblock	Gridgen	Modified SA	JAXA Murayama
G	CFL3D-Thin	Multiblock	Tinoco	SA	Boeing Tinoco
H	CFL3D-Thin	Multiblock	Tinoco	SST	Boeing Tinoco
I	CFL3D-Full	Multiblock	Tinoco	SA	Boeing Tinoco
J	CFL3D-Full	Multiblock	Tinoco	SST	Boeing Tinoco
K	CFL3D-Full	Overset	Sclafani	SST	LaRC Rumsey
L	CFL3D-Thin	Overset	Sclafani	SST	LaRC Rumsey
M	Overflow	Overset	Sclafani	SA	Boeing Sclafani
N	TAU	Hybrid	DLR	SA Edwards	DLR Brodersen
O	Edge	Hybrid	ANSYS CFX	Hellsten EARSM	FOI Eliason
P	FUN3D	Unstructured	LaRC Nodal	SA	LaRC Lee–Rausch
Q	NSU3D	Hybrid	LaRC Mixed	SA	UWy Mavriplis
R	CFD + +	Hybrid	AFLR	SA	Boeing Venkat
S	BCFD	Hybrid	AFLR	SA	Boeing Winkler
T	UPACS	Multiblock	Gridgen	SST	JAXA Murayama
U	OVERFLOW	Overset	Sclafani	SST	LaRC Rumsey
V	FLUENT	Unstructured	Embraer	K-Epsilon	Fluent Scheidigger
W	STAR-CCM+	Unstructured	STAR	SST	CD-Adapco Vaughn
X	USM3D	Unstructured	USM3D	SA/WF	Raytheon Venkat
Y	BCFD	Hybrid	AFLR	SST	Boeing Winkler
Z	TAS	Unstructured	TAS	Modified SA	JAXA Murayama

V. Results

Participants of the DPW-III were required to provide results on either the wing/body or wing-alone test case. To their credit, many participants chose to investigate both cases; several provided multiple data sets on a given case. This section summarizes the data collected on these test cases. These data are then used to estimate absolute drag levels for the DLR-F6 with and without the FX2B fairing, and lift-to-drag ratios of the DPW-W1 and DPW-W2 wings. These estimates are made before any experimental data are available (at test-case Reynolds number) on any of the configurations. There were 26 submissions for case 1 and 11 for case 2. To help minimize confusion, the case 1 submissions are tagged with a single capitalized letter from A–Z, while the case 2 submissions are labeled 1–11. The following sections detail the results for the two cases.

A. Case 1: DLR-F6 WB with and Without FX2B Fairing

The first test case is the DLR-F6 wing/body configuration with and without the FX2B fairing. Table 3 provides the CFD code, grid type, grid family, turbulence model, and submitter name and organization for each block of data submitted. Twenty of the 26 submissions were complete in the sense that they included all of the mandatory data requested. Although almost all of the data were supplied by the six remaining, these data blocks could not be used to conduct a consistent Richardson extrapolation to the continuum in the grid-sensitivity study.

A representative example of the wing pressure distributions at the design condition of $M = 0.75$, $C_L = 0.5$, and $Re = 5 \times 10^6$ is given in Fig. 2. In this example, the 15% semispan (near side of body) upper-surface pressure distribution of the baseline DLR-F6 clearly exhibits signs of flow separation, while the flow about the FX2B geometry is well attached. In general, the DPW-III submissions unanimously agreed that the flow was well attached for the FX2B configuration, however, they were divided dramatically on the size of the side-of-body separation bubble for the baseline DLR-F6. More discussion on this will follow.

1. *Case 1a: Fixed-C_L Single-Point Grid-Sensitivity Study*

Figures 3–6 provide grid-sensitivity trends for idealized profile drag at the single-point fixed-C_L condition. In these figures, side-by-side comparison plots are shown, where the baseline DLR-F6 data are captured in the left plot and the FX2B data on the right. The curves of these plots are labeled with the tag letter given in Table 3. Note that all data blocks based on the Tinoco grid family also include results from a medium–fine grid; for consistency, these data are not included in the tables, nor were they used in the ranking procedure described at the end of this section. Figure 3 includes all data from all submissions. At first glance of this overview plot, the scatter in this data can be quite disheartening. Recall that the medium mesh is supposed to represent the current engineering practice. In these figures, the medium mesh grid factor falls within the range (2E-05, 3E-05). Hence, the range of the idealized profile drag scatter of the current engineering practice is on the order of 50 counts, for either configuration. A paper by Morrison and Hemsch [44] addresses this scatter and better quantifies confidence levels through a rigorous statistical analysis of the data.

The composite curves of Fig. 3 are broken out by grid type in Figs. 4–6. Figure 4 illustrates the trend of the multiblock CFD results. In this figure, note that three different multiblock families are shown. The solid lines represent results using the Tinoco grid

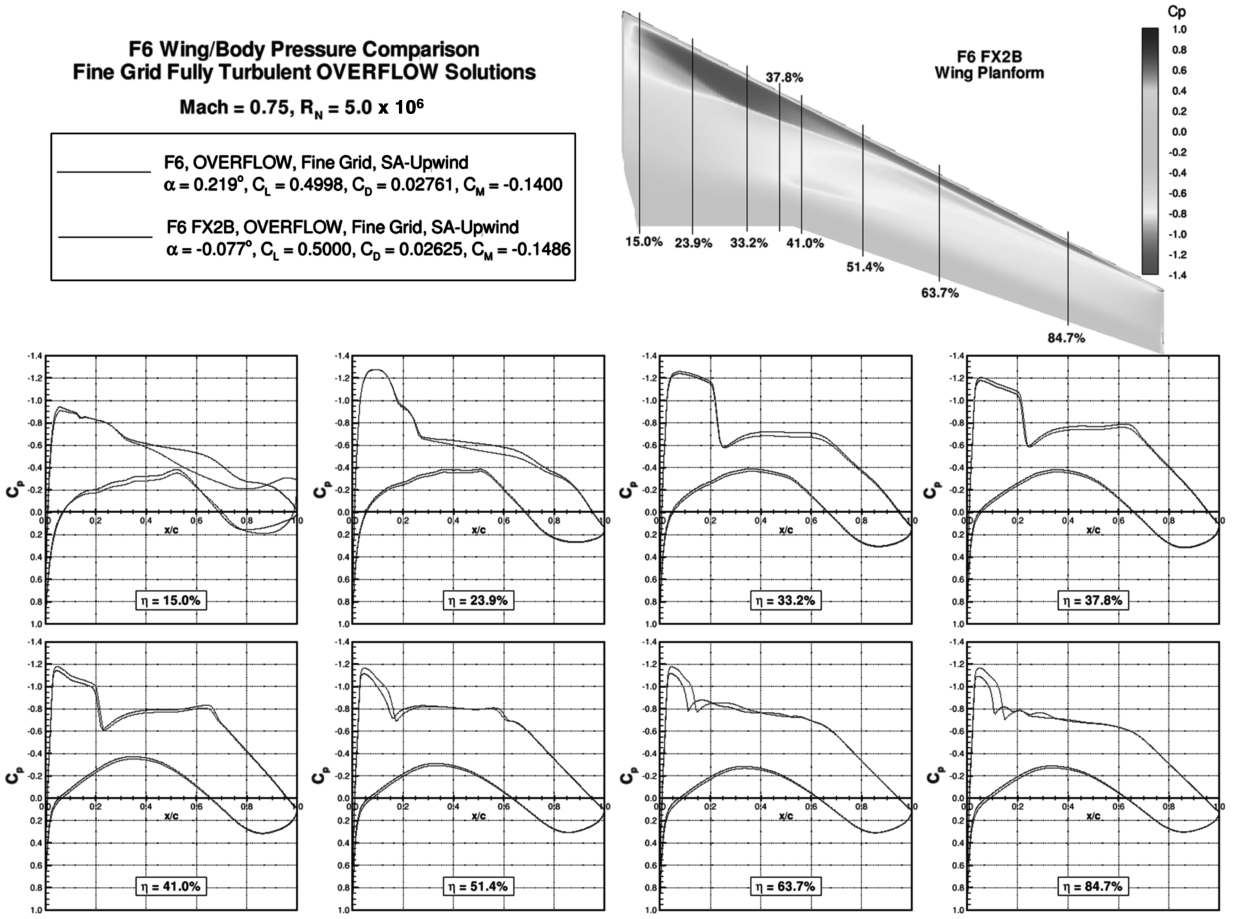

Fig. 2 Comparison of pressure distributions on the DLR-F6 wing/body: $M = 0.75$, $C_L = 0.5$, and $Re = 5 \times 10^6$.

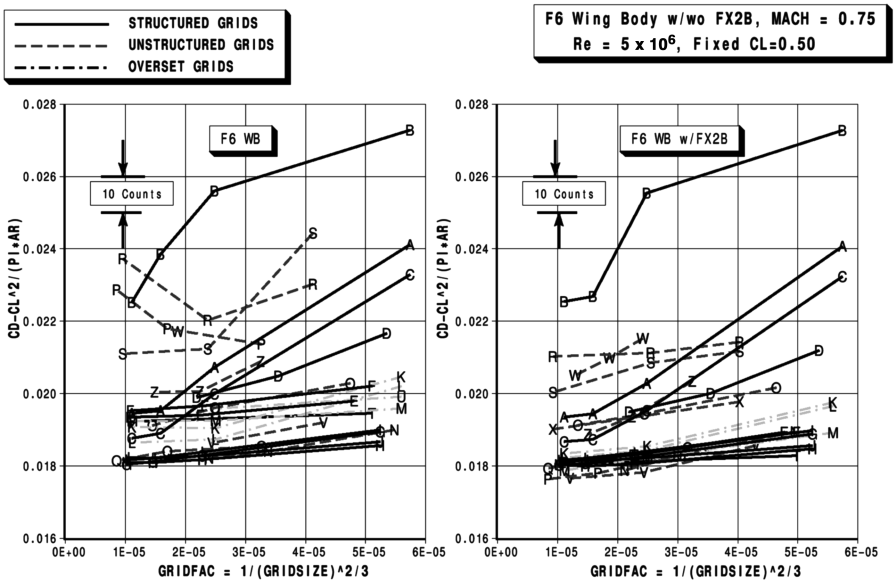

Fig. 3 Case 1 grid sensitivity on idealized profile drag: $M = 0.75$, $C_L = 0.5$, and $Re = 5 \times 10^6$.

family; the dashed lines capture the Gridgen families; the chain-dot refers to the SAUNA grid family. For the DLR-F6 baseline, note that if extrapolated to the continuum, many of the Tinoco-grid-family results indicate a low-drag value, while the Gridgen-grid-family data point to a higher value. For the FX2B geometry, the data associated with these two grid families are more comparable. Figure 5 shows the grid-sensitivity trends for the Sclafani grid family of overset-grid results. Figure 6 provides the corresponding trends of the unstructured and hybrid CFD solutions. In this figure, note that the unstructured-mesh families are grouped. The solid lines represent results based on the LaRC grid families; the dashed lines depict results using the AFLR grid families; the chain-dot lines capture data based on the five remaining unstructured-mesh families.

Figure 7 illustrates the size and location of the side-of-body separation bubble for the baseline DLR-F6 wing/body configuration,

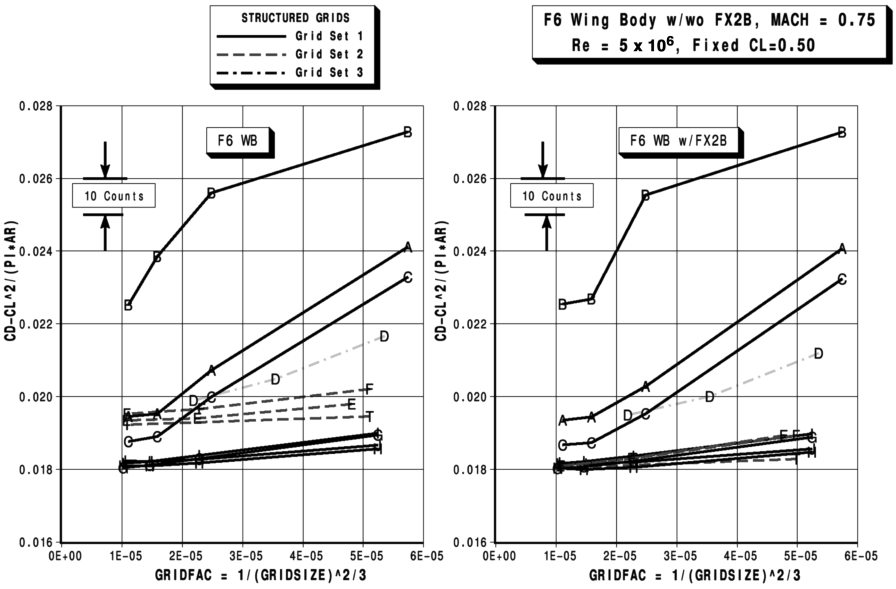

Fig. 4 Case 1 grid sensitivity on structured-mesh idealized profile drag.

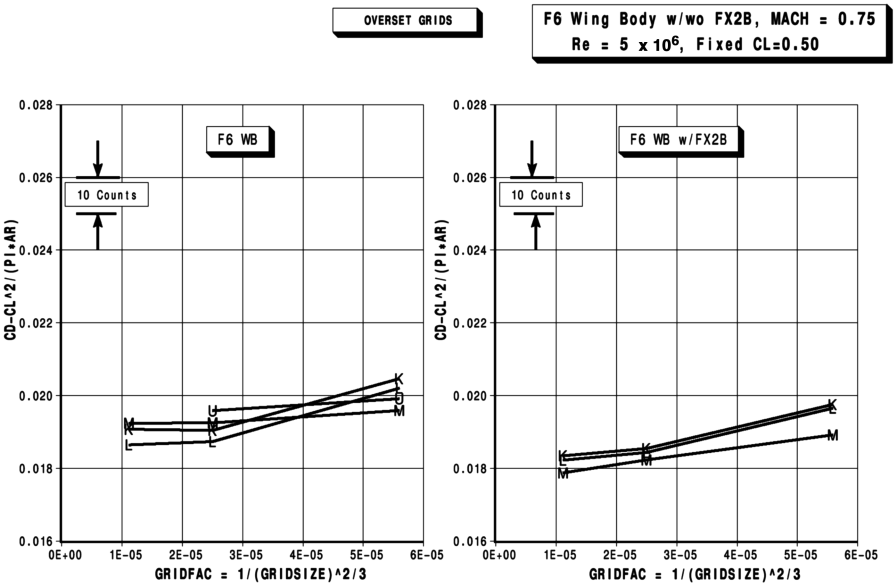

Fig. 5 Case 1 Grid Sensitivity on overset-mesh idealized profile drag.

as computed by the participants. The airflow is from left to right, the bold vertical line depicts the wing trailing edge, while the bold curved horizontal line is the wing/body intersection. The A–Z symbols plotted in this figure represent the (X-EYE,Y-EDGE) coordinates of the computed separation bubbles. Here, X-EYE depicts the streamwise position of the bubble eye (which is approximately the streamwise location of the maximum bubble width), and Y-EDGE is the maximum spanwise extent of the bubble. For reference, these data are overlayed on an oil-flow pattern taken from an ONERA wind-tunnel test. However, note that the oil-flow pattern of the test corresponds to a lower Reynolds-number flow. For clarity, these data are organized into three subplots by grid type. This figure illustrates that there is large scatter in the computed sizes of the separation bubble, represented by Y-EDGE, even within the common grid types.

Upon reviewing the previous five figures, it appears visually that some of the grid-convergence data may be classified as outliers. How to quantify a block of data as an outlier can be a rather tricky matter. Nonetheless, there is an enormous amount of information encoded in the database provided by the participants and presented previously in Figs. 3–6. See Morrison and Hemsch [44] for one approach to identify outliers through statistical filtering, and Vassberg [33] for another technique based on the linearity of convergence trend lines.

If a Richardson extrapolation is performed on a pair of data from a grid-sensitivity curve, an estimate of the continuum value is obtained. If this extrapolation is performed using data from the fine and medium meshes, the resulting value does not necessarily equal that of a similar extrapolation using data from the medium and coarse meshes. If the two values are equal, the trend line is exactly straight, and thus meets the necessary (but insufficient) requirement that data from all three meshes fall within an asymptotic range. For the constant-lift grid sensitivity of case 1, this type of extrapolation could be performed on α, C_D, $C_{D\text{pr}}$, $C_{D\text{sf}}$, or C_M. In the following Lagrange equation, let $\mathcal{Y}$ represent any one of these quantities, and $\mathcal{X} = N^{-\frac{2}{3}}$. Here, N is the total number of grid points in the grid system. As defined, $\mathcal{X}$ is an appropriate parameter for a second-order scheme applied to results on a parametric family of three-dimensional meshes that have been uniformly refined in all three coordinate directions.

$$\mathcal{Y}_{FM} = \frac{\mathcal{X}_M \mathcal{Y}_F - \mathcal{X}_F \mathcal{Y}_M}{\mathcal{X}_M - \mathcal{X}_F}$$

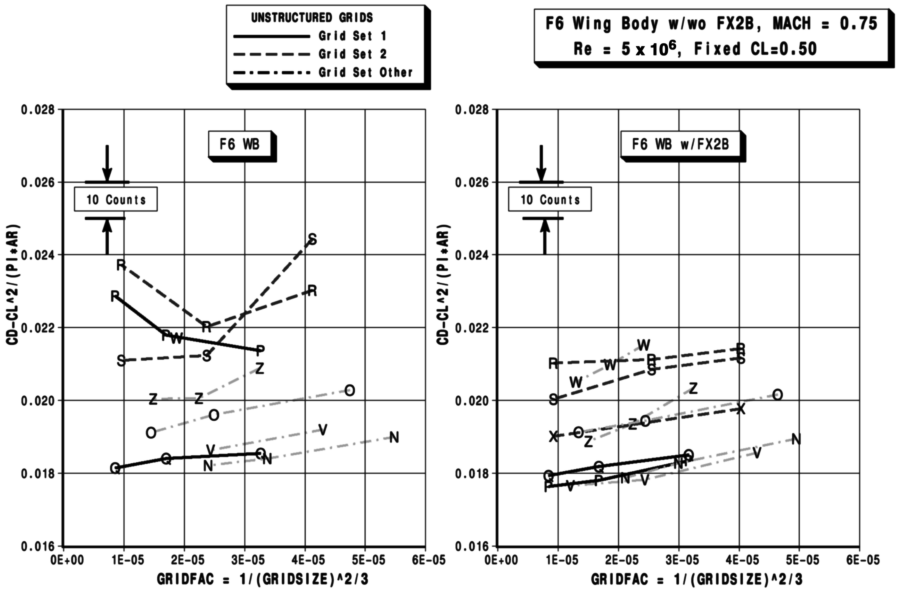

Fig. 6 Case 1 grid sensitivity on unstructured-mesh idealized profile drag.

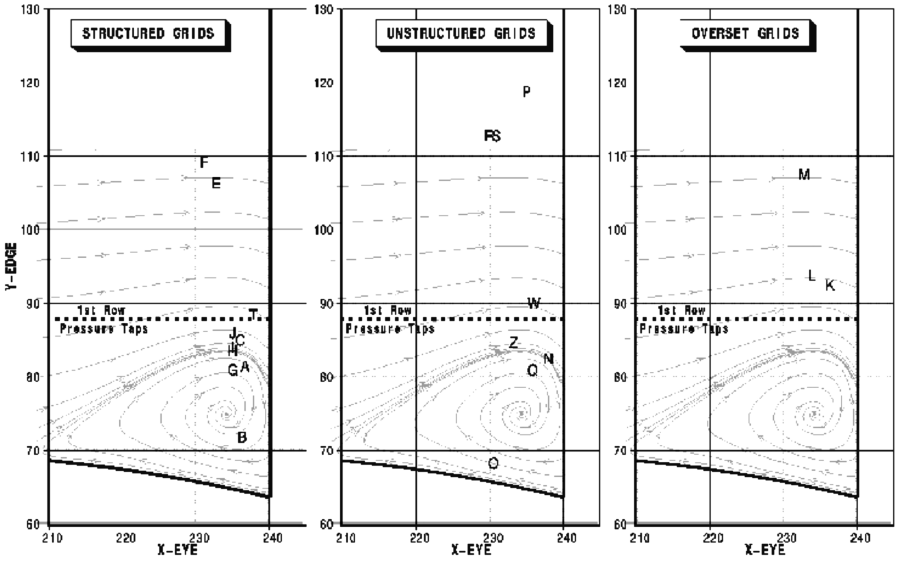

Fig. 7 Case 1 side-of-body separation bubble characteristics of the baseline DLR-F6.

Table 4 Case 1 DLR-F6 data extrapolated to continuum

Tag	α	C_D	$C_{D\text{pr}}$	$C_{D\text{sf}}$	C_M	$C_D - C_L^2/(\pi\text{AR})$
A	0.0244	0.02686	0.01404	0.01283	−0.14617	0.01843
B	−0.0614	0.02846	0.01420	0.01425	−0.15065	0.02005
C	0.1518	0.02613	0.01428	0.01185	−0.13747	0.01778
D	−0.0990	0.02732	0.01470	0.01261	−0.15342	0.01894
E	0.1824	0.02761	0.01552	0.01209	−0.14624	0.01930
F	0.2003	0.02772	0.01564	0.01208	−0.14602	0.01941
G	−0.1633	0.02622	0.01392	0.01231	−0.15753	0.01784
H	0.0472	0.02641	0.01438	0.01203	−0.14280	0.01803
I	−0.0909	0.02636	0.01402	0.01235	−0.14770	0.01799
J	0.0863	0.02658	0.01453	0.01205	−0.13211	0.01820
K	0.2692	0.02747	0.01544	0.01205	−0.13538	0.01910
L	0.0737	0.02795	0.01485	0.01210	−0.14450	0.01857
M	0.2663	0.02759	0.01561	0.01199	−0.13944	0.01923
N	0.1022	0.02612	0.01335	0.01252	−0.15245	0.01775
O	0.0400	0.02710	0.01375	0.01334	−0.16255	0.01844
P	1.2476	0.03226	0.02193	0.01035	−0.11064	0.02396
Q	0.1006	0.02626	0.01473	0.01151	−0.14349	0.01788
R	−1.1783	0.03325	——	——	——	0.02487
S	0.4938	0.02939	0.01740	0.01199	−0.12926	0.02101
Z	−0.1089	0.02846	0.01628	0.01215	−0.15433	0.02002

Table 5 Case 1 DLR-F6 data extrapolated to continuum

Tag	α	C_D	$C_{D\text{pr}}$	$C_{D\text{sf}}$	C_M	$C_D - C_L^2/(\pi\text{AR})$
A	0.1296	0.02701	0.01409	0.01293	−0.13977	0.01860
B	0.0950	0.02854	0.01430	0.01422	−0.14129	0.02013
C	0.2210	0.02639	0.01438	0.01199	−0.13328	0.01798
D	−0.1150	0.02705	0.01427	0.01275	−0.15310	0.01867
E	−0.0887	0.02628	0.01393	0.01235	−0.15479	0.01790
F	−0.888	0.02628	0.01391	0.01237	−0.15489	0.01790
G	−0.0569	0.02624	0.01382	0.01244	−0.15189	0.01786
H	0.1178	0.02639	0.01423	0.01217	−0.13818	0.01802
I	−0.0673	0.02636	0.01388	0.01251	−0.14343	0.01798
J	0.1180	0.02655	0.01437	0.01220	−0.13562	0.01818
K	0.0507	0.02656	0.01438	0.01220	−0.14227	0.01818
L	0.0493	0.02643	0.01425	0.01220	−0.14353	0.01805
M	−0.0907	0.02596	0.01366	0.01230	−0.14997	0.01759
N	−0.1414	0.02527	0.01324	0.01202	−0.16042	0.01691
O	0.3866	0.02584	0.01505	0.01077	−0.11826	0.01746
P	0.3866	0.02584	0.01505	0.01077	−0.11826	0.01746
Q	0.2634	0.02606	0.01444	0.01161	−0.13338	0.01768
R	−0.0405	0.02934	——	——	——	0.02097
S	0.1207	0.02795	0.01569	0.01226	−0.13778	0.01957
Z	−0.1140	0.02627	0.01397	0.01228	−0.15451	0.01789

Here, $\mathcal{Y}_{FM}$ represents the continuum estimates using the fine/medium pairs of data.

Unfortunately, the level to which the uniform-refinement critereon has been achieved varies across the set of baseline grid families. For structured meshes, this requirement can be easily met by uniformly scaling the I, J, and K dimensions. For unstructured meshes, the situation is more complicated. One approach is to use a global scaling parameter related to cell sizes, but this technique is difficult to enforce uniformly and does not guarantee the mesh connectivity to be self-similar between coarse and fine meshes. Another approach is to subdivide each element into smaller elements, but this can lead to undesirable cell aspect ratios, especially in the finest grid.

Twenty of the submissions provided sufficient data to perform a consistent set of Richardson extrapolations. These data are summarized in Table 4 for the baseline DLR-F6 and in Table 5 for the FX2B configuration. The estimated continuum values in these tables are based on fine/medium mesh extrapolations. (Note that these tables omit all medium–fine data based on the Tinoco grids so that comparison across data blocks is more consistent.)

Before leaving the discussion related to the continuum estimates, a couple of observations will be noted; there are a few back-to-back comparisons in the data where only one variable changed. For example, the drag predicted using the full Navier–Stokes equations appears to be higher than that obtained using the thin-layer approximations. The back-to-back comparisons yielding this observation come from the data block pairs of (G, I), (H, J), and (L, K) for both the DLR-F6 and FX2B results; all six pairs exhibit this trend.

Another comparison that can be made is regarding the Spallart–Allmaras (SA) and shear stress transport (SST) (mentor) turbulence models. Here refer to the data block pairs of (G, H), (I, J), and (M, U). Although we do not have sufficient data for a continuum estimate of the U data block, we can compare the DLR-F6 medium grid results with those of the M data block. In this comparison, all five pairs of data show that the total drag from the SST model is higher than that from the SA model. Digging further into this SA/SST comparison shows that the pressure drag of the SST model is always higher than that of the SA model, yet the skin-friction drag shows the opposite trend in all cases.

In addition to the above trends identified, other trends are currently being investigated by participants of the DPW-III with postworkshop studies. As an example, Sclafani [41] studied the effect of an extreme refinement of the grid near the wing trailing edge. Also, he added an extra-fine mesh to his overset grid families; the results on

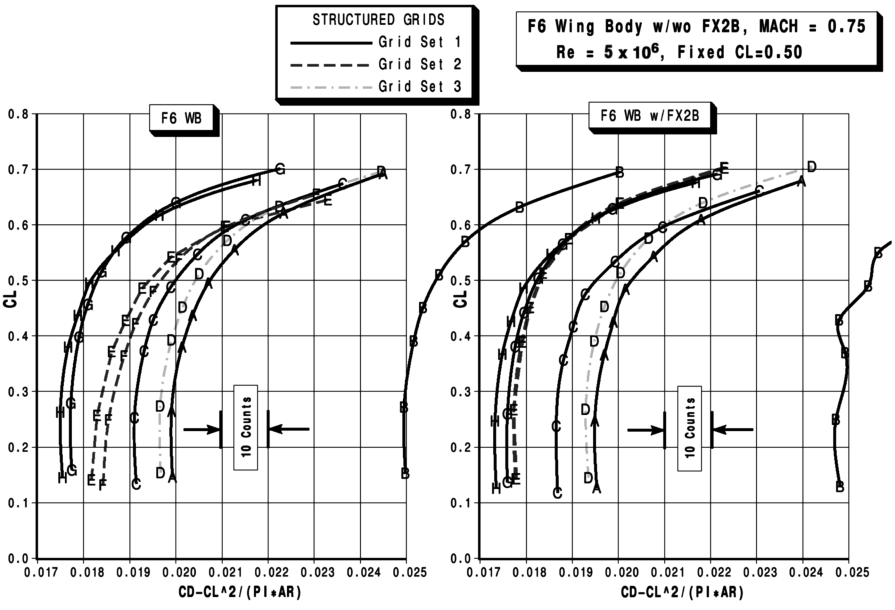

Fig. 8 Case 1 structured-mesh idealized profile drag polars.

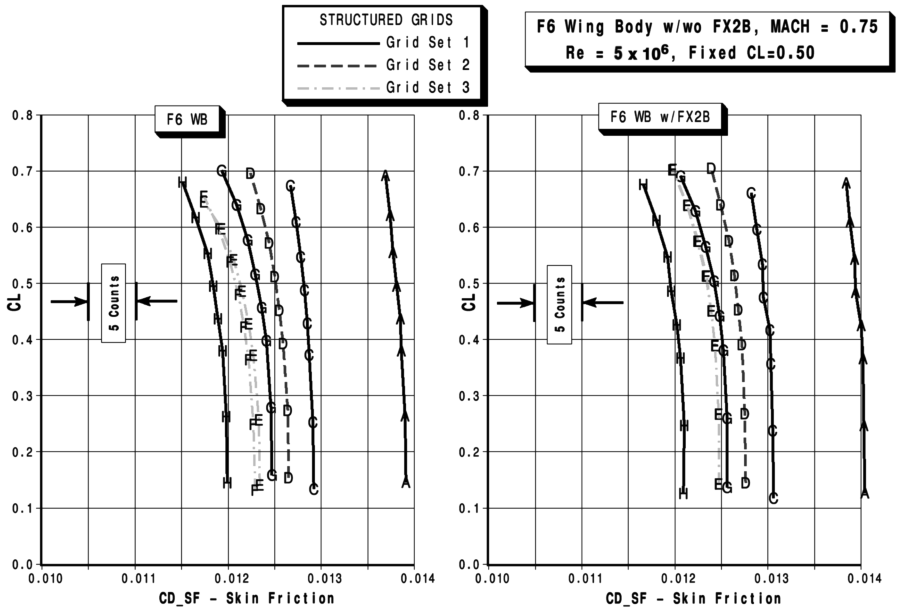

Fig. 9 Case 1 structured-mesh skin-friction polars.

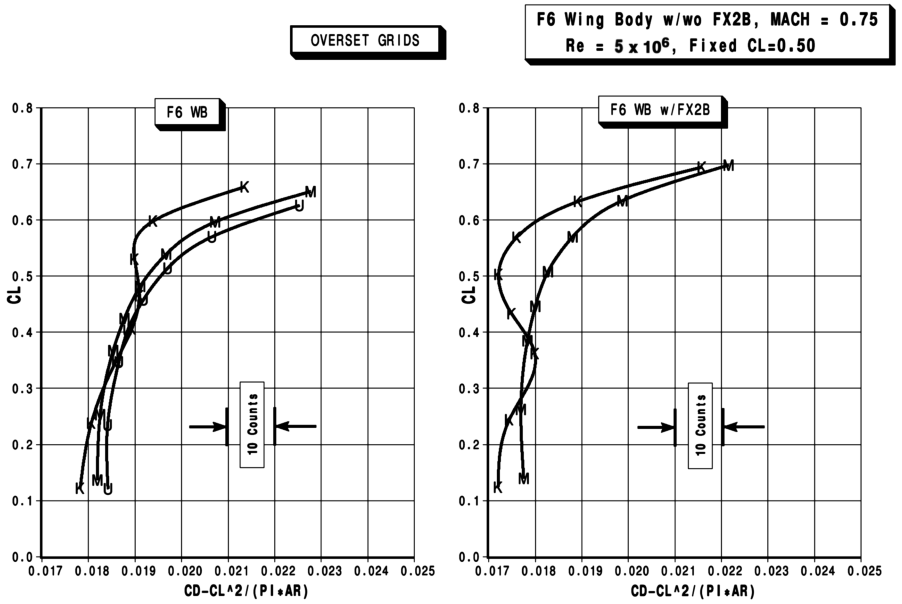

Fig. 10 Case 1 overset-mesh idealized profile drag polars.

the baseline DLR-F6 show that the side-of-body bubble monotonically grows with increasing grid refinement. Further, the size of the bubble is consistently larger when the flow is computed with the full Navier–Stokes equations as compared with that of the thin-layer approximations.

2. Case 1b: Drag Polar on Medium Grid Study

The remainder of this section provides the α-sweep data. For clarity, these data are presented by grid type using similar side-by-side plots as before, with DLR-F6 on the left and FX2B on the right.

Figures 8 and 9 provide the idealized profile drag and skin-friction drag, respectively, of the data blocks based on multiblock structured grids. Note that these curves have been further itemized by grid family sets. The solid lines represent results using the Tinoco grid families; the dashed lines capture the Gridgen families; the chain dot refers to the SAUNA grid families. In these figures, data block B appears to be an outlier related to the idealized profile drag, and data block A looks like an outlier with respect to skin friction.

Figures 10 and 11 provide drag-polar results based on the overset mesh family. Note that the shapes of the idealized profile drag polars for the K data block are unlike those of any other data block. Upon further inspection, it was noticed that the grid-sensitivity data from the K submission were not compatible with its own polars. The cause of this inconsistency was tracked down to different processes being used to compute the fixed-C_L results from those of the α sweep. As a consequence, these data are updated in a companion paper [41] focused on overset-mesh drag predictions.

Figures 12 and 13 address the unstructured and hybrid mesh data. These data are also grouped. The solid lines represent results based on the LaRC grid families; the dashed lines depict results using the AFLR grid families; the chain-dot lines capture data based on the five remaining unstructured-mesh families. Here, the S and P data blocks appear to be outliers on the DLR-F6 idealized profile drag polars; the S block is also an extreme on the FX2B scatter. Refering to the skin-friction polars, the P and W data blocks look like they could also be outliers.

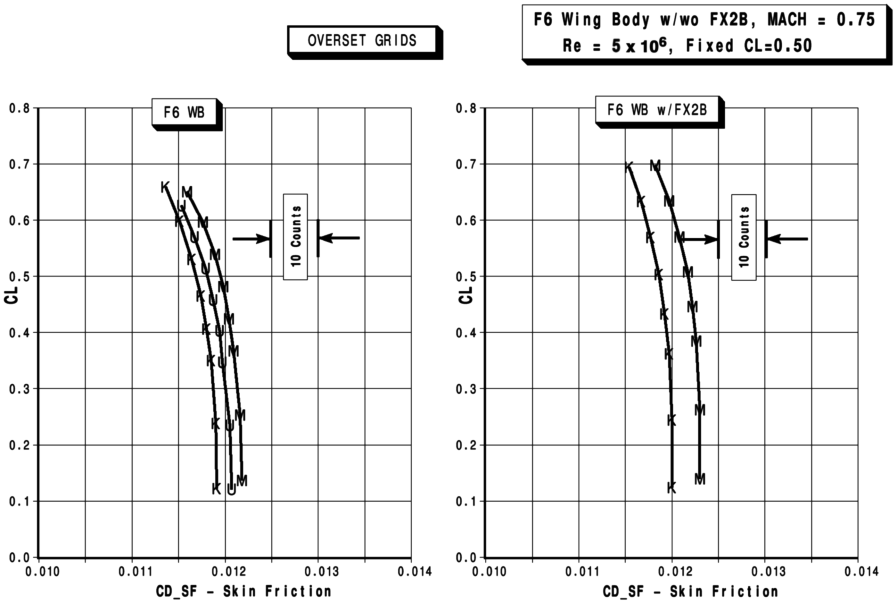

Fig. 11 Case 1 overset-mesh skin-friction polars.

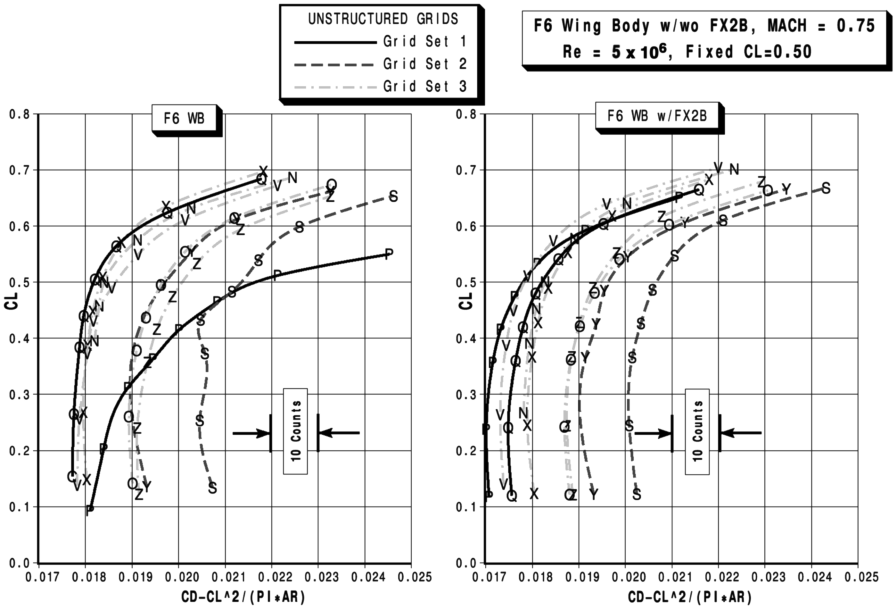

Fig. 12 Case 1 unstructured-mesh idealized profile drag polars.

For completeness, lift and pitching-moment curves are included next. Figure 14 shows the lift curves. Here, note that the P data block appears to be an outlier on the DLR-F6 lift curve. Figure 15 shows the pitching-moment curves. Here, none of the pitching-moment curves clearly stand out as being outliers.

B. Case 2: DPW–W1/W2 Wing Alone

The second test case is based on the wing-alone geometries developed by the organizing committee. Table 6 provides the CFD code, grid type, grid family, turbulence model, and submitter name and organization for each block of data submitted. Ten of the 11 submissions were complete in the sense that they included all of the mandatory data requested. These data were used to conduct a consistent Richardson extrapolation to the continuum in the grid-sensitivity study that follows.

A representative example of the DPW-W1 wing pressures and upper-surface streamlines at the design condition of $M = 0.76$, $\alpha = 0.5$ deg, and $Re = 5 \times 10^6$ is given in Figs. 16 and 17. Figure 17 overplots the 55% semispan pressure distributions as computed on the coarse, medium, fine, and extra-fine meshes. Notice that there is an almost imperceptible difference of these pressures between all but the coarse mesh solution. This behavior is typical of all of the data submitted on this case to the DPW-III.

1. Case 2a: Fixed-α Single-Point Grid-Sensitivity Study

Figures 18–23 provide grid-sensitivity trends for the single-point constant-α condition of $M = 0.76, \alpha = 0.5$ deg, and $Re = 5 \times 10^6$. These figures are organized such that the W1 data reside on the left side of the page and the W2 data on the right. All curves are labeled with a number 1–9,0. Recall that this grid-sensitivity study includes four meshes.

Figures 18 and 19 illustrate the grid convergence of total drag. The scatter of these curves is on the order of 10% and is fairly constant with grid resolution. Figures 20 and 21 depict the trends of lift with respect to grid resolution. The scatter of these curves is also on the order of 10%. However, because drag is a strong function of lift, and lift varies between data blocks, maybe the scatter on predicted aerodynamic performance is not as large as it seems in Figs. 18 and

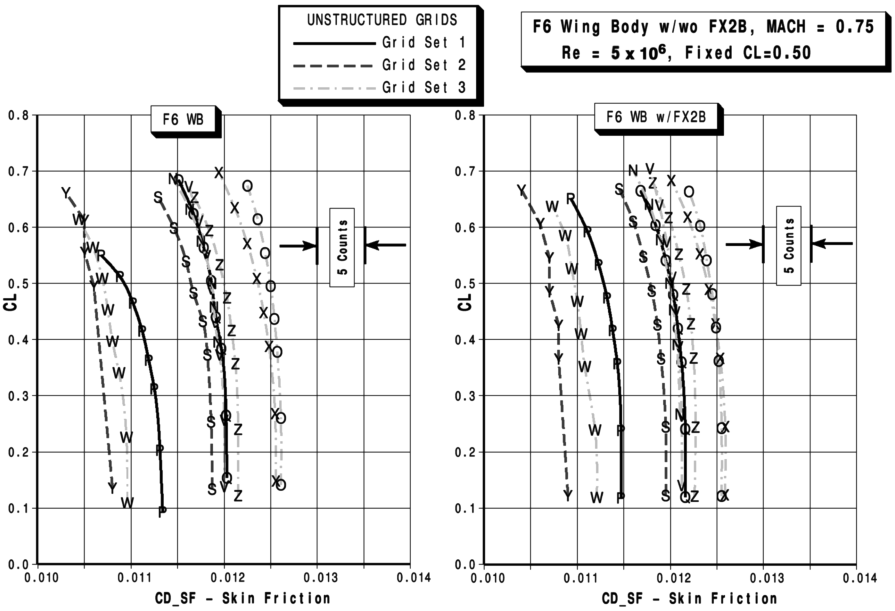

Fig. 13 Case 1 unstructured-mesh skin-friction polars.

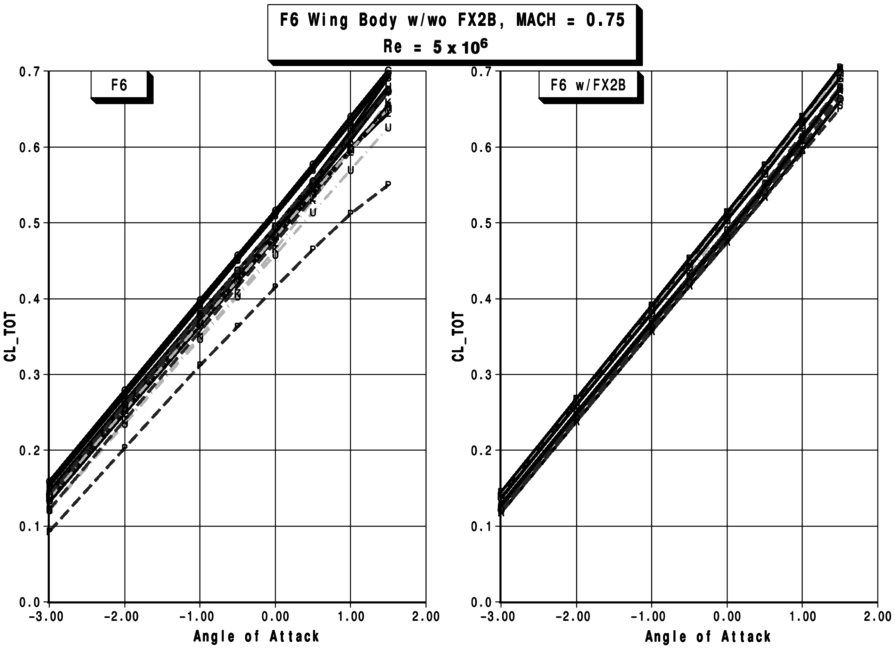

Fig. 14 Case 1 lift curves.

19. In an attempt to compensate for drag variation due to lift, the next two metrics are included. Figures 22 and 23 illustrate the idealized profile drag trend lines. Notice that the scatter band of this metric has been reduced to about 5% of absolute drag. Figures 24 and 25 depict the lift-to-drag (L/D) ratio of these data. Again, the scatter is about 5% of absolute L/D. Although the scatter bands of the later two metrics are better than those of lift and drag, they are only comparable to the scatter bands of the wing/body configurations of case 1.

The continuum estimates of the $\mathcal{Y}_{XF}$ extrapolations are summarized in Table 7 for the DPW-W1 wing and in Table 8 for the DPW-W2 wing. Here, $\mathcal{Y}_{XF}$ represents the continuum estimates using the extra-fine/fine pairs of data.

2. *Case 2b: Drag Polar on Medium Grid Study*

Figures 26 and 27 provide the polar of idealized profile drag, C_{DP}, for DPW-W1 and DPW-W2, respectively. Notice that the DPW-W1 polar has a typical parabolic shape, while the DPW-W2 polar exhibits a drag-bucket behavior. This characteristic is common for single-point optimizations in a low-dimension design space. In these medium grid drag polars, at the higher lifting conditions, data block 6 consistently shows a higher idealized profile drag than that of the other data blocks.

Figures 28 and 29 illustrate the computed lift curves. Note the linear behavior of the DPW-W1 wing lift curve for $-1 \leq \alpha \leq 1$ deg. In this same α range, note the nonlinear behavior of the DPW-W2 wing lift curve. The scatter bands of both sets of lift curves are about $\Delta C_L \sim 0.04$ in size. The roundover of these curves occurs at $\alpha \geq 1.5$ deg. The lift curve of data block 6 is on the low extreme side of the set.

Figures 30 and 31 show the pitching-moment trends with angle of attack. With the exception of data block 9, the shapes of these curves are very similar. The pitching-moment curve of data block 6 is on the high extreme side of these data.

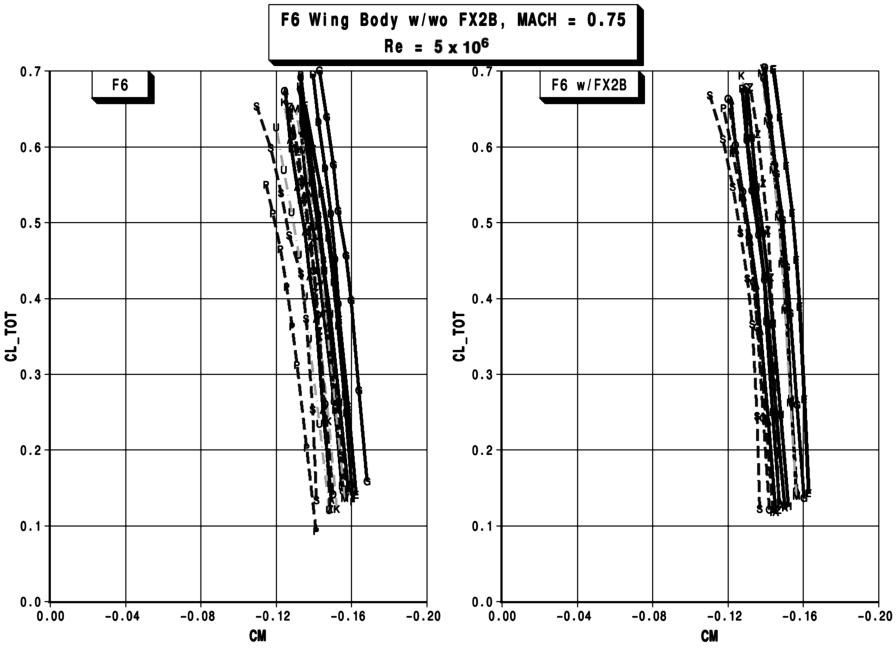

Fig. 15 Case 1 pitching-moment curves.

Table 6 Case 2 submissions

Tag	Code	Grid type	Grid type	Turbulence model	Submitter
1	FLUENT	Multiblock	Tinoco	K-Epsilon	Fluent Scheidigger
2	CFL3D-Thin	Multiblock	Tinoco	SA	Boeing Tinoco
3	CFL3D-Thin	Multiblock	Tinoco	SST	Boeing Tinoco
4	OVERFLOW	Overset	Sclafani	SA	Boeing Tinoco
5	TAU	Hybrid	DLR	SA Edwards	DLR Brodersen
6	FUN3D	Unstructured	LaRC Nodal	SA	LaRC Lee-Rausch
7	NSU3D	Hybrid	LaRC Mixed	SA	UWy Mavriplis
8	NSU3D	Unstructured	Raytheon	SA	Cessna Zickuhr
9	FLOWer	Multiblock	Tinoco	RSM	DLR Eisfeld
10	FLOWer	Multiblock	Tinoco	SST	DLR Raddatz
11	TAI	Multiblock	JFLO C-H	BL	TAI Tarhan

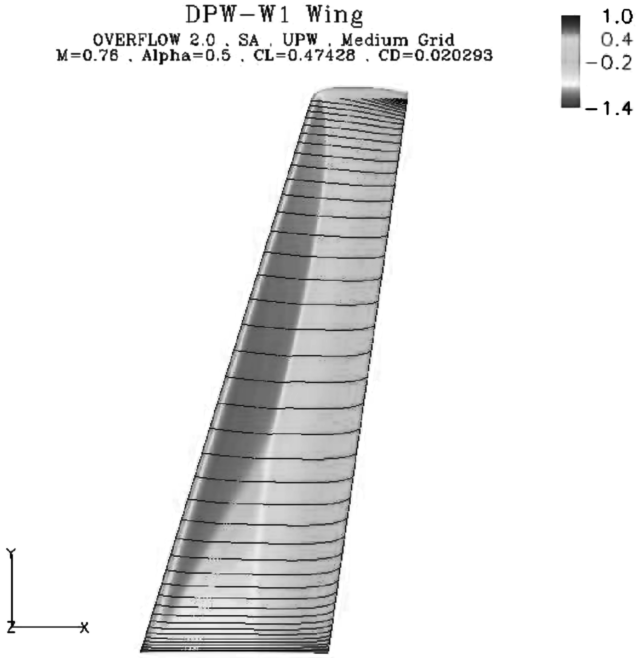

Fig. 16 Case 2 W1 upper-surface pressures and streamlines: $M = 0.76$, $\alpha = 0.5$ deg, and $Re = 5 \times 10^6$.

3. General Observation

A general observation, after reviewing all of the results, is that there is a set of CFD codes whose members all seem to agree relatively well with each other, and do so over all of the test cases spanning the DPW series. Most noteworthy about this core set of codes is that it is composed of flow solvers that are based on all types of grids.

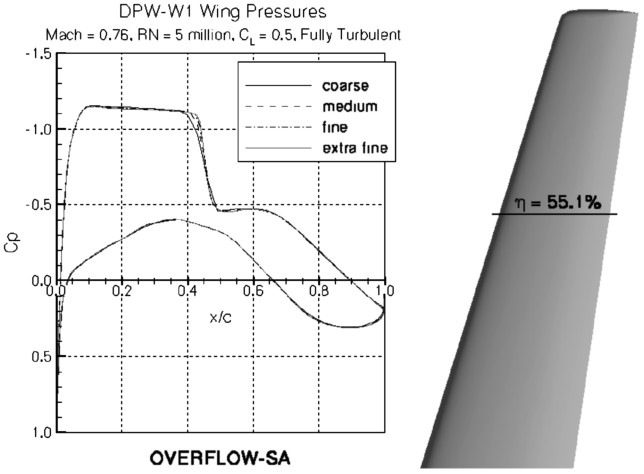

Fig. 17 Case 2 W1 pressure distributions: $M = 0.76$, $C_L = 0.5$, and $Re = 5 \times 10^6$.

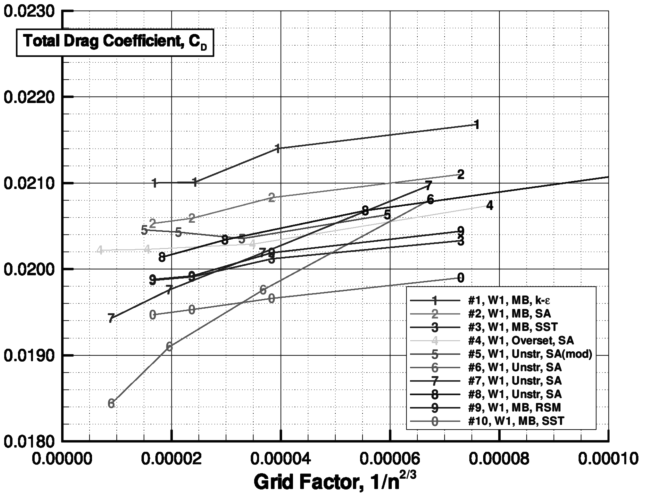

Fig. 18 Case 2 grid sensitivity on W1 total drag: $M = 0.76$, $\alpha = 0.5$ deg, and $Re = 5 \times 10^6$.

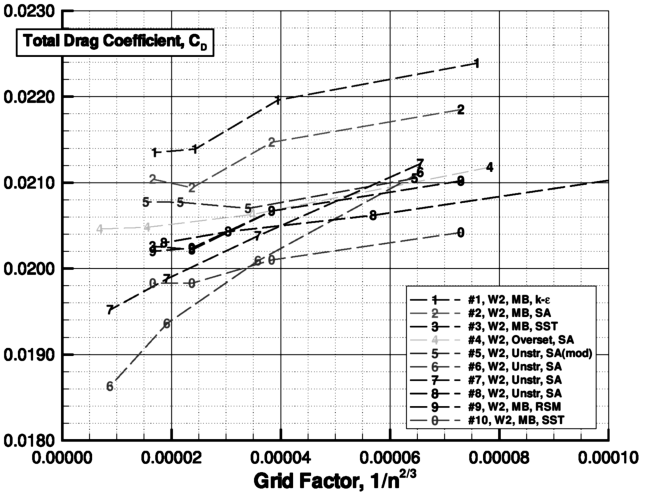

Fig. 19 Case 2 grid sensitivity on W2 total drag: $M = 0.76$, $\alpha = 0.5$ deg, and $Re = 5 \times 10^6$.

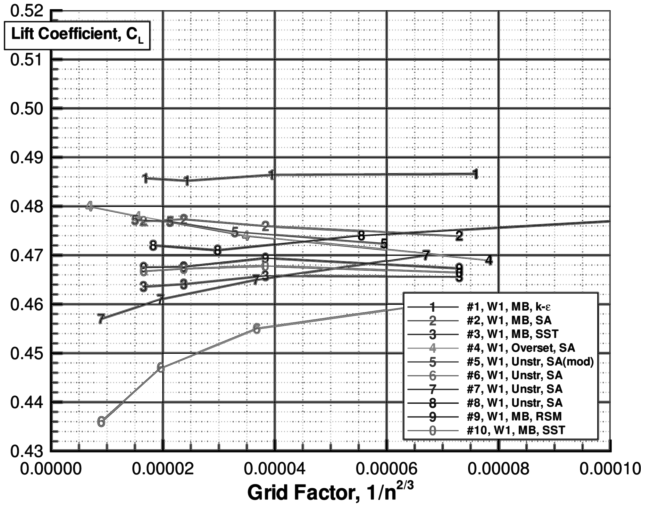

Fig. 20 Case 2 grid sensitivity on W1 lift: $M = 0.76$, $\alpha = 0.5$ deg, and $Re = 5 \times 10^6$.

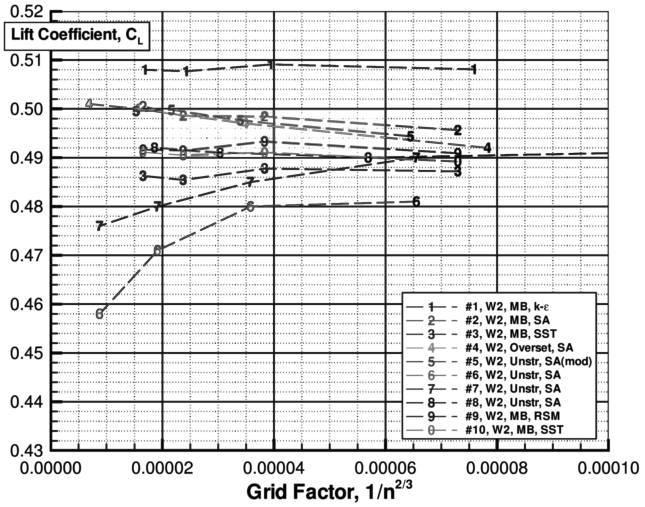

Fig. 21 Case 2 grid sensitivity on W2 Lift: $M = 0.76, \alpha = 0.5$ deg, and $Re = 5 \times 10^6$.

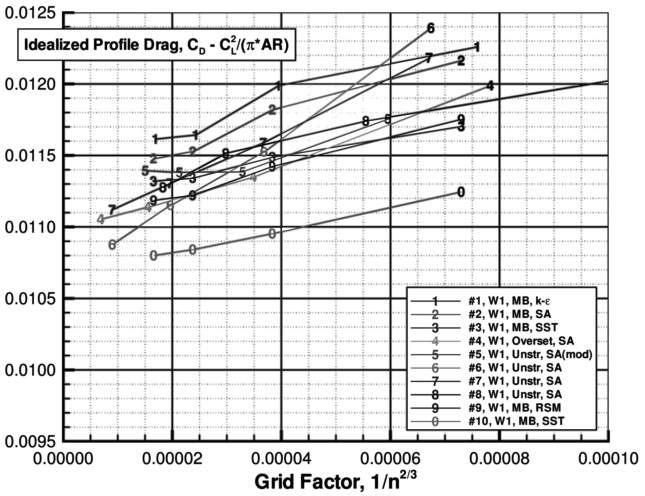

Fig. 22 Case 2 grid sensitivity on W1 idealized profile drag: $M = 0.76$, $\alpha = 0.5$ deg, and $Re = 5 \times 10^6$.

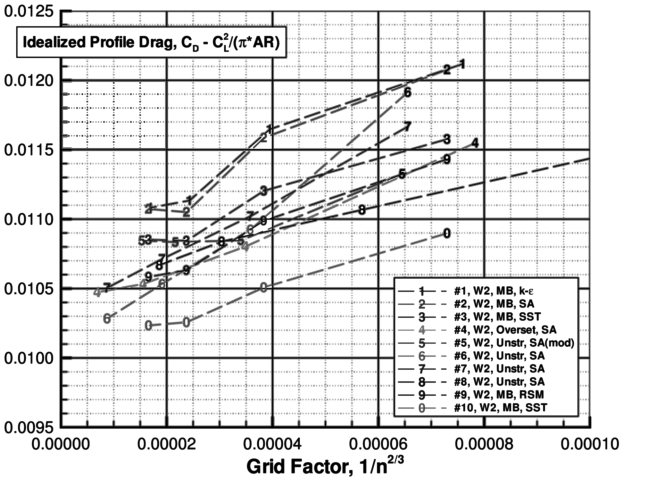

Fig. 23 Case 2 grid sensitivity on W2 idealized profile drag: $M = 0.76$, $\alpha = 0.5$ deg, and $Re = 5 \times 10^6$.

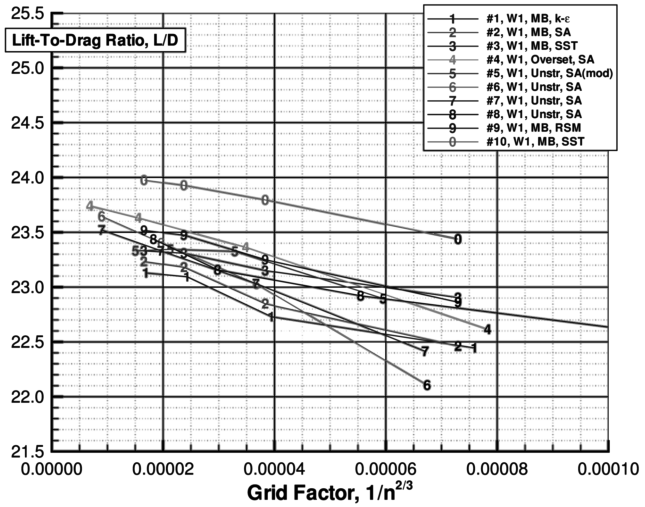

Fig. 24 Case 2 grid sensitivity on W1 lift-to-drag ratio: $M = 0.76$, $\alpha = 0.5$ deg, and $Re = 5 \times 10^6$.

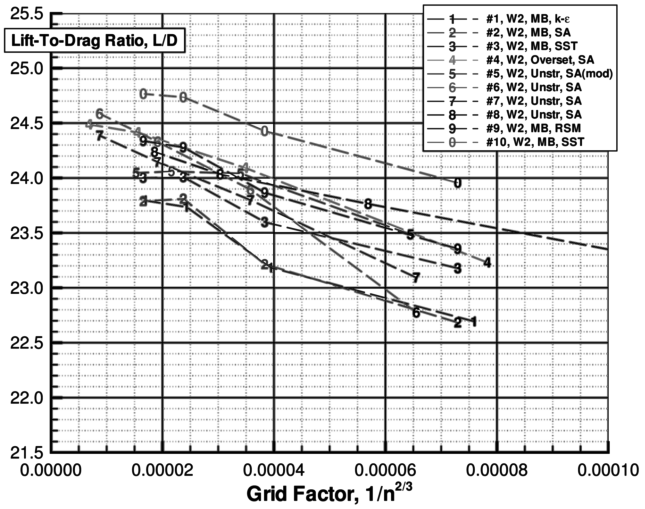

Fig. 25 Case 2 grid sensitivity on W2 lift-to-drag ratio: $M = 0.76$, $\alpha = 0.5$ deg, and $Re = 5 \times 10^6$.

VI. On-Going Plans

Work has been underway at NASA, at DLR, and by committee members for a September 2007 test of a refurbished DLR-F6 model in NASA's National Transonic Facility (NTF). The goal of the test is to provide data for comparison to existing DPW-III calculations with and without the Boeing-designed side-of-body fairing and at a Reynolds number higher than in the current database. DLR has provided all model hardware, including the new side-of-body fairing and mounting block to attach to the NASA balance. NASA has provided instrumentation, new model support hardware to closely match the ONERA hardware used in earlier tests, and NTF test time. The maximum Reynolds number is 5×10^6 based on mean aerodynamic chord, due to load limitations on the model and support hardware, and because the model is not suitable for cryogenic conditions. The test matrix includes 3×10^6 Reynolds-number runs to match existing data, with Mach numbers from 0.4 to 0.8. The clean-wing configuration with and without the new side-of-body fairing is included. Data to be acquired include forces, moments, surface pressures, and wing deformations under load. Targeted flow visualization will include transition measurements via sublimating chemicals, and techniques to visualize the side-of-body and wing trailing-edge flow separations.

Another collaboration currently being pursued by the organizing committee is related to the preparation of future workshops. A recurring theme of these events has consistently identified that the quality of the CFD results is only as good as the quality of the underlying meshes. The linkage between grid quality and solution quality has been recognized for decades. Nonetheless, it has been very difficult for the organizing committee to guarantee that all baseline meshes meet a consistent level of quality. To help address this issue, the committee has engaged dialog with the AIAA Meshing, Visualization, and Computational Environments (MVCE) Technical Committee to develop a more rigorous process of quality control for the standard baseline grids. This has resulted in planning a special session on grid generation before the next drag prediction

Table 7 Case 2 DPW-W1 data extrapolated to continuum

Tag	C_L	C_D	$C_{D\text{pr}}$	$C_{D\text{sf}}$	C_M	$C_D - C_L^2/(\pi\text{AR})$	L/D
1	0.48684	0.02098	0.01467	0.00631	−0.06970	0.01155	23.21
2	0.47626	0.02039	0.01430	0.00615	−0.6740	0.01137	23.36
3	0.46245	0.01978	0.01375	0.00603	−0.06390	0.01127	23.38
4	0.48160	0.02021	0.01422	0.00600	−0.06822	0.01098	23.83
5	0.47803	0.02052	0.01460	0.00592	−0.06774	0.01143	23.30
6	0.42668	0.01788	0.01245	0.00544	−0.05470	0.01064	23.86
7	0.45361	0.01788	0.01324	0.00592	−0.06172	0.01096	23.69
8	0.47359	0.01982	0.01398	0.00581	−0.06544	0.01090	23.89
9	0.46727	0.01979	0.01399	0.00580	−0.06491	0.01110	23.61
10	0.46564	0.01979	0.01382	0.00554	−0.01070	0.01070	23.61

Table 8 Case 2 DPW-W2 data extrapolated to continuum

Tag	C_L	C_D	$C_{D\text{pr}}$	$C_{D\text{sf}}$	C_M	$C_D - C_L^2(\pi\text{AR})$	L/D
1	0.50869	0.02126	0.01498	0.00628	−0.06920	0.01096	23.93
2	0.50491	0.02127	0.01517	0.00610	−0.06857	0.01113	23.74
3	0.48817	0.02035	0.01435	0.00599	−0.06434	0.01087	23.99
4	0.50180	0.02044	0.01448	0.00597	−0.06726	0.01043	24.54
5	0.49894	0.02078	0.01491	0.00589	−0.06384	0.01087	24.01
6	0.44704	0.01801	0.01261	0.00540	−0.05362	0.01007	24.82
7	0.47263	0.01922	0.01333	0.00589	−0.06003	0.01033	24.59
8	0.49359	0.02009	0.01429	0.00580	−0.06533	0.01040	24.56
9	0.49206	0.02011	0.01437	0.00574	−0.06490	0.01047	24.47
10	0.49249	0.01983	0.01434	0.00550	−0.06488	0.01018	24.84

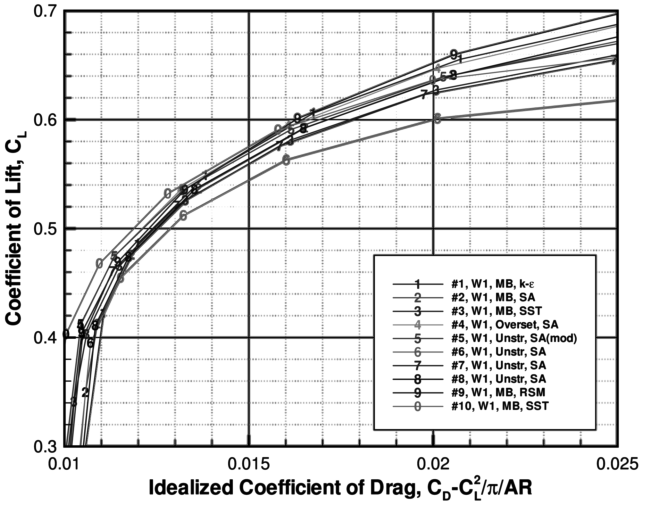

Fig. 26 Case 2 W1 idealized profile drag polar: $M = 0.76$, $Re = 5 \times 10^6$, medium mesh.

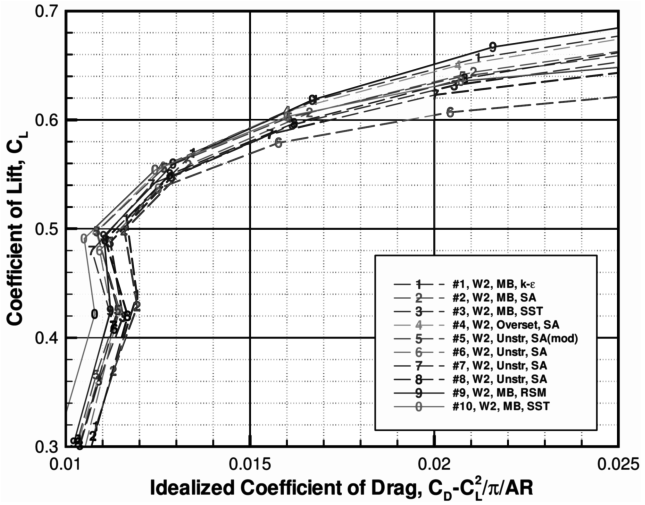

Fig. 27 Case 2 W2 idealized profile drag polar: $M = 0.76$, $Re = 5 \times 10^6$, medium mesh.

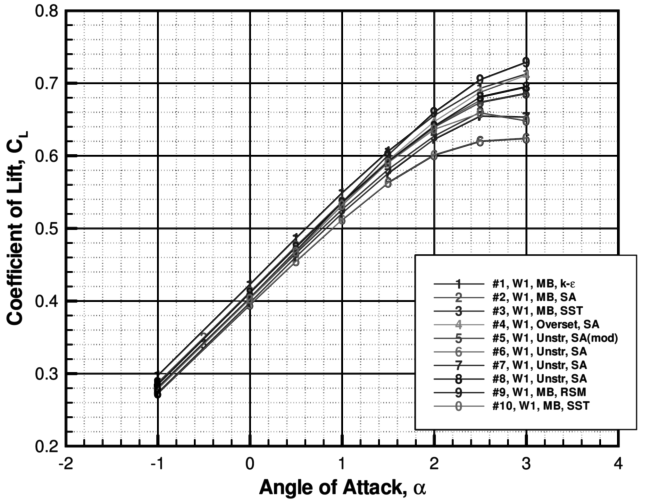

Fig. 28 Case 2 W1 C_L-α curves: $M = 0.76$, $Re = 5 \times 10^6$, medium mesh.

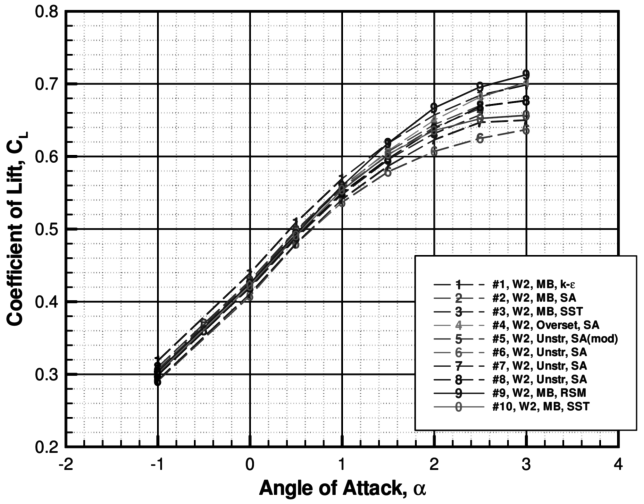

Fig. 29 Case 2 W2 C_L-α curves: $M = 0.76$, $Re = 5 \times 10^6$, medium mesh.

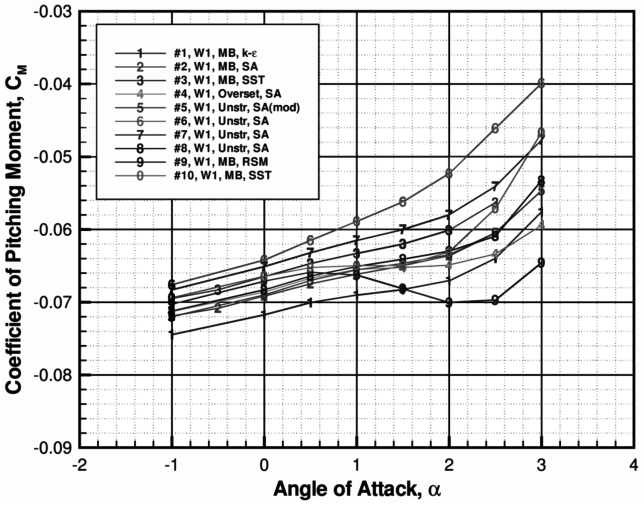

Fig. 30 Case 2 W1 C_M-α curves: $M = 0.76$, $Re = 5 \times 10^6$, medium mesh.

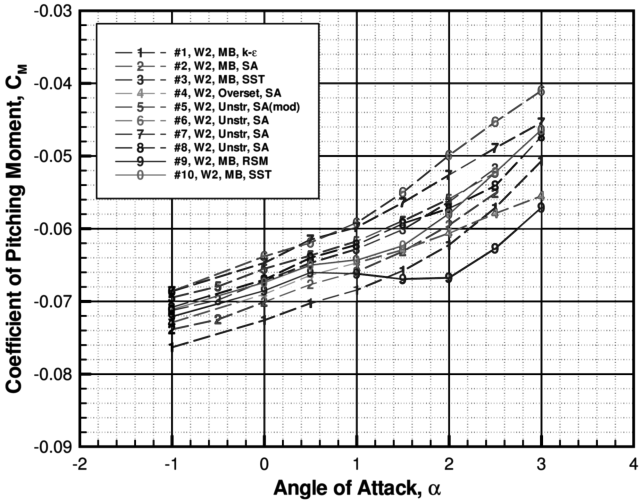

Fig. 31 Case 2 W2 C_M-α curves: $M = 0.76$, $Re = 5 \times 10^6$, medium mesh.

workshop where the baseline grids will officially be made available to the public domain, and quality metrics of these grids are formally documented and discussed in an open forum.

VII. Conclusions

Results from the Third AIAA Drag Prediction Workshop are summarized. This workshop focused on the prediction of drag for wing-body and wing-alone configurations that are representative of transonic transport aircraft. Numerical calculations were performed using industry-relevant test cases. Numerous Reynolds-averaged Navier–Stokes CFD results on fully turbulent flows are provided. These solutions are performed on structured, unstructured, and hybrid grid systems. The structured grid sets include point-matched multiblock meshes and overset grid systems. The unstructured and hybrid grid sets are composed of tetrahedral, pyramid, and prismatic elements. Effort was made to provide a high-quality and parametrically consistent family of grids for each grid type about each configuration under study. The wing-body families are composed of a coarse, medium, and fine grid, while the wing-alone families also include an extra-fine mesh. These mesh sequences are used to help determine how the provided flow solutions fare with respect to asymptotic grid convergence, and are used to estimate an absolute drag of each configuration.

The DPW series has provided a very broad view of the state of the art of CFD applications within the industry, much more so than that which can be garnered by an isolated study. In fact, by reviewing in isolation any one of the DPW-III's individual data blocks, one may arrive at different conclusions than those presented herein. For example, a typical publication may show how successful a CFD solution matches test data. By combining a large set of solutions from many sources around the world, this workshop clearly shows that there remains much room for improvement. Although this conclusion is somewhat disappointing, it is tempered by an observation that there exists a core set of CFD methods that consistently agree with each other in general, and do so on all test cases spanning the workshop series. Most noteworthy about this core set of solvers is that these methods are based on all grid types.

A measure of merit is introduced that quantifies issues specifically associated with grid-convergence data. This metric is not biased by grid type, absolute value of drag, or slope of grid-convergence trend line. It does not identify the source of a problem, only that a problem exists with the grid-convergence data. Applied to the data blocks of DPW-III, this metric successfully identified which data blocks were outliers, at least at the flow condition of the grid-convergence studies.

Through the data compiled by this workshop, it is obvious that several problematic issues continue to persist in the processes used for accurate drag prediction. Generating a consistent set of grids for the purpose of grid-convergence studies remains a challenge, especially for unstructured meshes. The side-of-body separation bubble of the DLR-F6 wing/body configuration continues to be a source of difficulty; the full set of CFD solutions shows a large variation of predicted bubble sizes. However, on a good note, the skin-friction predictions of the aggregate data blocks are well behaved and form relatively tight groupings.

An underlying objective of the DPW-III was to test a hypothesis that pockets of flow separation can be a root cause of poor grid-convergence characteristics. Although it appears that pockets of flow separation did adversely affect the grid-convergence trends of many of the CFD data blocks provided by the participants, it did not seem to cause issues with others. This is somewhat of an unexpected finding of the DPW-III.

Acknowledgments

The authors thank the AIAA Applied Aerodynamics Technical Committee for sponsoring the Drag Prediction Workshop Series. We also thank our respective organizations for their continued support in this endeavor. A special thanks is extended to the participants of DPW-III, for without their contributions, this workshop would not have been possible. Finally, the planning of these workshops throughout the duration of the series has been conducted by a substantial number of dedicated individuals. Members of the aggregate organizing committees include Shreekant Agrawal, Olaf Brodersen, Bob Dowgwillo, Bernhard Eisfeld, Jean Luc Godard, Mike Hemsch, Steve Klausmeyer, Kelly Laflin, Dave Levy, Mori Mani, Rick Matus, Dimitri Mavriplis, Joe Morrison, Bas Oskam, Shahyar Pirzadeh, Mark Rakowitz, Ed Tinoco, John Vassberg, Rich Wahls, and Tom Zickuhr.

References

[1] 1st AIAA CFD Drag PredictionWorkshop, http://aaac.larc.nasa.gov/tsab/cfdlarc/aiaa-dpw/Workshop1/workshop1.html, June 2001 [retrieved 14 Dec. 2007].

[2] Redeker, G., "DLR-F4 Wing-Body Configuration," *A Selection of Experimental Test Cases for the Validation of CFD Codes*, AGARD AR-303, Aug. 1994, pp. B4.1–B4.21.

[3] Vassberg, J. C., DeHaan, M. A., and Sclafani, A. J., "Grid Generation Requirements for Accurate Drag Predictions Based on OVERFLOW Calculations," AIAA Paper 2003-4124, June 2003.

[4] Levy, D. W., Vassberg, J. C., Wahls, R. A., Zickuhr, T., Agrawal, S., Pirzadeh, S., and Hemsch, M. J., "Summary of Data from the First AIAA CFD Drag Prediction Workshop," AIAA Paper 2002-0841, Jan. 2002.

[5] Levy, D. W., Vassberg, J. C., Wahls, R. A., Zickuhr, T., Agrawal, S., Pirzadeh, S., and Hemsch, M. J., "Summary of Data from the First AIAA CFD Drag Prediction Workshop," *Journal of Aircraft*, Vol. 40, No. 5, pp. 875–882, Sept.–Oct. 2003.

[6] Hemsch, M. J., "Statistical Analysis of CFD solutions from the Drag Prediction Workshop," AIAA Paper 2002-0842, Jan. 2002.

[7] Hemsch, M. "Statistical Analysis of CFD Solutions from the Drag Prediction Workshops," *CFD-Based Aircraft Drag Prediction and Reduction*, von Karman Institute Lecture Series, von Karman Institute, Nov. 2003.

[8] Rakowitz, M., Eisfeld, B., Schwamborn, D., and Sutcliffe, M., "Structured and Unstructured Computations on the DLR-F4 Wing-Body Configuration," AIAA Paper 2002-0837, Jan. 2002.

[9] Rakowitz, M., Eisfeld, B., Schwamborn, D., and Sutcliffe, M., "Structured and Unstructured Computations on the DLR-F4 Wing-Body Configuration," *Journal of Aircraft*, Vol. 40, No. 2, 2003, pp. 256–264.

[10] Mavriplis, D. J., and Levy, D. W. "Transonic Drag Predictions Using an Unstructured Multigrid Solver," AIAA Paper 2002-0838, Jan. 2002.

[11] Pirzadeh, S. Z., and Frink, N. T. "Assessment of the Unstructured Grid Software TetrUSS for Drag Prediction of the DLR-F4 Configuration," AIAA Paper 2002-0839, Jan. 2002.

[12] Vassberg, J. C., Buning, P. G., and Rumsey, C. L., "Drag Prediction for the DLR-F4 Wing/Body Using OVERFLOW and CFL-3D on an Overset Mesh," AIAA Paper 2002-0840, Jan. 2002.

[13] 2nd AIAA CFD Drag Prediction Workshop, http://aaac.larc.nasa.gov/tsab/cfdlarc/aiaa-dpw/, dpw@cessna.textron.com, June 2003 [retrieved 14 Dec. 2007].

[14] Laflin, K. R., Vassberg, J. C., Wahls, R. A., Morrison, J. H., Brodersen, O., Rakowitz, M., Tinoco, E. N., and Godard, J., "Summary of Data from the Second AIAA CFD Drag Prediction Workshop," AIAA Paper 2004-0555, Jan. 2004.

[15] Laflin, K. R., Vassberg, J. C., Wahls, R. A., Morrison, J. H., Brodersen, O., Rakowitz, M., Tinoco, E. N., and Godard, J., "Summary of Data from the Second AIAA CFD Drag Prediction Workshop," *Journal of Aircraft*, Vol. 42, No. 5, 2005, pp. 1165–1178.

[16] Hemsch, M., and Morrison, J. "Statistical Analysis of CFD Solutions from the Second Drag Prediction Workshop," AIAA Paper 2004-0556, Jan. 2004.

[17] Pfeiffer, N. "Reflections on the Second Drag Prediction Workshop," AIAA Paper 2004-0557, Jan. 2004.

[18] Brodersen, O., Rakowitz, M., Amant, S., Larrieu, P., Destarac, D., and Sutcliffe, M. "Airbus, ONERA, and DLR Results from the Second AIAA Drag Prediction Workshop," AIAA Paper 2004-0391, Jan. 2004.

[19] Brodersen, O. P., Rakowitz, M., Amant, S., Larrieu, P., Destarac, D., and Suttcliffe, M., "Airbus, ONERA and DLR Results from the Second AIAA Drag Prediction Workshop," *Journal of Aircraft*, Vol. 42, No. 4, 2005, pp. 932–940.

[20] Langtry, R. B., Kuntz, M., and Menter, F. "Drag Prediction of Engine-Airframe Interference Effects with CFX-5," AIAA Paper 2004-0392, Jan. 2004.

[21] Langtry, R. B., Kuntz, M., and Menter, F. "Drag Prediction of Engine-Airframe Interference Effects with CFX-5," *Journal of Aircraft*, Vol. 42, No. 6, 2005, pp. 1523–1529.

[22] Sclafani, A. J., DeHaan, M. A., and Vassberg, J. C., "OVERFLOW Drag Predictions for the DLR-F6 Transport Configuration: A DPW-II Case Study," AIAA Paper 2004-0393, Jan. 2004.
[23] Rumsey, C., Rivers, M., and Morrison, J. "Study of CFD Variations on Transport Configurations from the 2nd AIAA Drag Prediction Workshop," AIAA Paper 2004-0394, Jan. 2004.
[24] Wutzler, K., "Aircraft Drag Prediction Using Cobalt," AIAA Paper 2004-0395, Jan. 2004.
[25] May, G., E. van derWeide, Jameson, A., and Shankaran, S., "Drag Prediction of the DLR-F6 Configuration," AIAA Paper 2004-0396, Jan. 2004.
[26] Kim, Y., Park, S., and Kwon, J., "Drag Prediction of DLR-F6 Using the Turbulent Navier-Stokes Calculations with Multigrid," AIAA Paper 2004-0397, Jan. 2004.
[27] Yamamoto, K., Ochi, A., Shima, E., and Takaki, R., "CFD Sensitivity to Drag Prediction on DLR-F6 Configuration by Structured Method and Unstructured Method," AIAA Paper 2004-0398, Jan. 2004.
[28] Tinoco, E., and Su, T., "Drag Prediction with the Zeus/CFL3D System," AIAA Paper 2004-0552, Jan. 2004.
[29] Klausmeyer, S., "Drag, Lift, and Moment Estimates for Transonic Aircraft Using the Navier-Stokes Equations," AIAA Paper 2004-0553, Jan. 2004.
[30] Lee-Rausch, E., Frink, N., Milholen, W., and Mavriplis, D. "Transonic Drag Prediction Using Unstructured Grid Solvers," AIAA Paper 2004-0554, Jan. 2004.
[31] 3rd AIAA CFD Drag Prediction Workshop, http://aaac.larc.nasa.gov/tsab/cfdlarc/aiaa-dpw/, dpw@cessna.textron.com, June 2006 [retrieved 14 Dec. 2007].
[32] Vassberg, J. C., Sclafani, A. J., and DeHaan, M. A., "A Wing-Body Fairing Design for the DLR-F6 Model: A DPW-III Case Study," AIAA Paper 2005-4730, June 2005.
[33] Vassberg, J. C., Tinoco, E. N., Mani, M., Brodersen, O. P., Eisfeld, B., Wahls, R. A., Morrison, J. H., Zickuhr, T., Laflin, K. R., and Mavriplis, D. J., "Summary of the Third AIAA CFD Drag Prediction Workshop," AIAA Paper 2007-0260, Jan. 2007.
[34] Baker, T. J., "Mesh Generation: Art or Science?," *Progress in Aerospace Sciences*, Vol. 1, No. 1, Jan. 2005, pp. 29–63. doi:10.1016/j.paerosci.2005.02.002
[35] Salas, M. D., "Digital Flight: The Last CFD Aeronautical Grand Challenge," *Journal of Scientific Computing*, Vol. 28, Nos. 2–3, Sept. 2006, pp. 479–505. doi:10.1007/s10915-006-9087-7
[36] Brodersen, O., and Sturmer, A., "Drag Prediction of Engine-Airframe Interference Effects Using Unstructured Navier-Stokes Calculations," AIAA Paper 2001-2414, June 2001.
[37] Samant, S. S., Bussoletti, J. E., Johnson, F. T., Burkhart, R. H., Everson, B. L., Melvin, R. G., and Young, D. P., "TRANAIR: A Computer Code for Transonic Analysis of Arbitrary Configurations," AIAA Paper 87-0034, Jan. 1987.
[38] Gill, P. E., Murray, W., Saunders, M. A., and Wright, M. H., "User's Guide for npsol (Ver. 4.0): A Fortran Package for Nonlinear Programming," Stanford University, TR SOL 86-2, Dept. of Operations Research, Jan. 1986.
[39] Gill, P. E., Murray, W., Saunders, M. A., and Wright, M. H., "Some Theoretical Properties of an Augmented Lagrangian Merit Function," *Advances in Optimization and Parallel Computing*, edited by P. M. Pardalos, North-Holland, Amsterdam, 1992, pp. 101–128.
[40] Tinoco, E. N., Winkler, C., Mani, M., and Venkatakrishnan, V. "Structured and Unstructured Solvers for the 3rd CFD Drag Prediction Workshop," AIAA Paper 2007-0255, Jan. 2007.
[41] Sclafani, A. J., Vassberg, J. C., Harrison, N. A., DeHaan, M. A., Rumsey, C. L., Rivers, S. M., and Morrison, J. H., "Drag Predictions for the DLR-F6 Wing/Body and DPW Wings Using CFL3D and OVERFLOW on an Overset Mesh, AIAA Paper 2007-0257, Jan. 2007.
[42] Mavriplis, D. J., "Results from the 3rd Drag Prediction Workshop Using the NSU3D Unstructured Mesh Solver," AIAA Paper 2007-0256, Jan. 2007.
[43] Brodersen, O., Eisfeld, B., Raddatz, J., and Frohnapfel, P., "DLR Results from the Third AIAA CFD Drag Prediction Workshop," AIAA Paper 2007-0259, Jan. 2007.
[44] Morrison, J. H., and Hemsch, M. J., "Statistical Analysis of CFD Solutions from the Third AIAA Drag Prediction Workshop," AIAA Paper 2007-0254, Jan. 2007.